VELOCE III. Reconstructing Radial Velocity Curves of Classical Cepheids

Giordano Viviani¹ and Richard I. Anderson¹

Institute of Physics, École Polytechnique Fédérale de Lausanne (EPFL), Observatoire de Sauverny, Chemin Pegasi 51b, 1290 Versoix, Switzerland

e-mail: giordano.viviani@epfl.ch, richard.anderson@epfl.ch

ABSTRACT

Switzerland
e-mail: giordano.viviani@epfl.ch, richard.anderson@ep
submitted: ; revised: ; accepted:

ABST

We present a novel framework for accurately reconstructing radial v
sampled time-series data suitable for application in large spectre
principal components of RV curves established based on high-preproject; template RV curves of Cepheids can be readily extracted
to estimate unbiased pulsation average velocities, v_y, to within 20
Subsampling the initial data set, we show that v_y and P2P can be
from as few as three observations. Expectedly, P2P is more sensit
time-series RV data of Cepheids in the Large and Small Magellani
root mean square errors of 0.5 – 2.0 km s⁻¹. The typical total une
providing sensitivity to spectroscopic binaries (SB). We identified
LMC and SMC, respectively. This yields a single-lined SB fracti
Way's SB fraction of 29% established as part of VELOCE. Despite t
line-of-sight component of the LMC's large-scale rotation, which
the SMC are more complex and not sufficiently sampled by the avand P2P of Cepheids observed by large spectroscopic surveys, su
into the kinematics and multiplicity of evolved intermediate-mass s
Key words. Stars: oscillations – Stars: variables: Cepheids – Tecl

1. Introduction

1. Introduction

1. Introduction

1. Introduction

2. Classical Cepheids are cornerstone objects in astrophysics. Their
radial pulsations cause periodic radius and temperature changes
observable as variations in light intensity, angular diameter, and
as spectral line shapes and positions. Radial velocity (RV) measurements based on high-resolution spectra encode fundamental
stellar properties and are useful, among other things, for determining the multiplicity of evolved intermediate-mass stars (cf.
Moe & Di Stefano 2017, for a review and Shetye et al. 2024;
Dinnbier et al. 2024 for Cepheids more specifically), calibrating and measuring distances via the Baade-Wesselink technique
(e.g., Storm et al. 2004; Nardetto et al. 2006, 2008; Anderson
2014; Gallenne et al. 2017; Trahin et We present a novel framework for accurately reconstructing radial velocity (RV) curves of classical Cepheids (Cepheids) from sparsely sampled time-series data suitable for application in large spectroscopic surveys. The framework provides a set of priors for the principal components of RV curves established based on high-precision measurements from the VELOcities of CEpheids (VELOCE) project; template RV curves of Cepheids can be readily extracted from our results. We demonstrate the ability of our framework to estimate unbiased pulsation average velocities, v_{γ} , to within $20-30 \text{ m s}^{-1}$, and peak-to-peak amplitudes, P2P, to within $\sim 2\%$. Subsampling the initial data set, we show that v_x and P2P can be determined to within ~ 0.35 km s⁻¹ and $\sim 6-7\%$, respectively, from as few as three observations. Expectedly, P2P is more sensitive to the number of observations, N_{RV} , than v_{γ} . We fitted existing time-series RV data of Cepheids in the Large and Small Magellanic Clouds (LMC, SMC) using this framework and obtained typical root mean square errors of $0.5 - 2.0 \text{ km s}^{-1}$. The typical total uncertainty on v_{γ} achieved for the SMC Cepheids is $\sim 0.85 \text{ km s}^{-1}$, providing sensitivity to spectroscopic binaries (SB). We identified 8 SB1 systems; two and one of which are new detections in the LMC and SMC, respectively. This yields a single-lined SB fraction of ~ 25% and 29% in the two galaxies, similar to the Milky Way's SB fraction of 29% established as part of VELOCE. Despite their relatively small number, LMC Cepheids reproduce the known line-of-sight component of the LMC's large-scale rotation, which differs in the extremes by more than 80 km s⁻¹. The kinematics of the SMC are more complex and not sufficiently sampled by the available Cepheids. Our framework is designed to yield accurate v_{γ} and P2P of Cepheids observed by large spectroscopic surveys, such as 4MOST, SDSS-V, and others, and will unlock new insights into the kinematics and multiplicity of evolved intermediate-mass stellar populations.

Key words. Stars: oscillations - Stars: variables: Cepheids - Techniques: radial velocities

(e.g., Storm et al. 2004; Nardetto et al. 2006, 2008; Anderson 2014; Gallenne et al. 2017; Trahin et al. 2021), and for understanding Galactic structure and kinematics (e.g., Pont et al. 1994; Mróz et al. 2019; Ablimit et al. 2020).

The advent of large time-resolved spectroscopic surveys enables the study of spectral variations in Cepheids in very large quantities, albeit typically with relatively few observations. A notable exception is the ESA Gaia mission (Prusti et al. 2016), which published time-series RV measurements based on the Ca II IR triplet for 715 Galactic Cepheids as part of the third Gaia data release (Gaia Collaboration et al. 2023; Katz et al. 2022; Ripepi et al. 2023, GDR3). Large spectroscopic surveys, notably the fifth installment of the Sloan Digital Sky Survey (Kollmeier et al. 2017, SDSS-V), WEAVE (Jin et al. 2024), the

4-metre Multi-Object Spectroscopic Telescope (de Jong et al. 2012, 4MOST) that recently saw first light, and future projects in development, such as the Wide-field Spectroscopic Telescope (Mainieri et al. 2024, WST) can generally acquire a few epochs per object but are not designed for cadenced time-series observations. In particular, the The One Thousand and One Magellanic Fields (1001MC) survey in 4MOST (Cioni et al. 2019) will collect high and low resolution spectra of ~ 9'000 Cepheids, with 3 – 6 visits planned in the central regions and an expected perepoch RV accuracy of $\sim 2 \,\mathrm{km \, s^{-1}}$. If accurate mean velocities of Cepheids can be established from such sparsely sampled RV curves, then extremely detailed line-of-sight velocity studies of the Magellanic Clouds (cf. van der Marel & Kallivayalil 2014; Jiménez-Arranz et al. 2023) will come within reach and complement proper motion-based studies (e.g., Niederhofer et al. 2022). Additionally, this will provide insights into possible differences among binary fractions across environments, galaxies, and metallicity regimes. Using Cepheids as precise tracers of kinematics requires considering their large-amplitude RV variations when determining the average, barycentric velocities, v_{ν} . Similar issues apply in the context of brightness variations in Cepheids (Kanbur et al. 2002; Tanvir et al. 2005; Yoachim et al. 2009; Bhardwaj et al. 2017; Bras et al. 2025) and other pulsating stars, such as RR Lyrae stars (Kanbur & Mariani 2004; Hajdu et al. 2018; Deb & Singh 2009; Paul & Chattopadhyay 2022), where mean magnitudes are often determined from sparsely

sampled light curves using template fitting. For RR Lyrae stars, several studies have furthermore constructed RV templates and analytic RV curve representations, (i.e. Liu 1991; Sesar 2012; Braga et al. 2021; Huang et al. 2024; Prudil et al. 2024). However, such an approach has thus far remained unfeasible in high detail for classical Cepheids due to the unavailability of sufficient data

The high-quality homogeneous RV time series published in the first data release of the VELOcities of CEpheids project (Anderson et al. 2024, henceforth VELOCE-I) provide a large and densely sampled reference data set for understanding Cepheid RV variations. In particular, VELOCE-I data have revealed new features of Cepheid RV curves (e.g., double bumps), allowed to determine the spectroscopic binary fraction of Galactic Cepheids (Shetye et al. 2024, henceforth VELOCE-II) and to assess the quality of GDR3 RV time series of Cepheids, and enabled the detection of a large zoo of modulation signals, some of which are explained by non-radial pulsations (Anderson 2014, 2016, 2019; Anderson et al. 2024; Netzel et al. 2024; Netzel et al. 2025; Barbey et al. 2025).

Here, we employed Principal Component Analysis (PCA) to establish the first high-fidelity framework for reconstructing classical Cepheid RV curves based on VELOCE-I. The PCA method is a dimensionality reduction technique frequently used in the creation of light and RV curve templates. It identifies a set of successive orthogonal components, called principal components (PCs), that sequentially maximize the explained variance within a given dataset of correlated variables (Pearson 1901; Hotelling 1933). Thus, PCA aims to pinpoint a subset of dimensions that can best re-express the given dataset as linear combination of the PCs (Shlens 2014). In practice, it allows to represent RV curves by a combination of projection coefficients. Templates are usually constructed by determining how these coefficients vary with a chosen set of physical parameters. This mapping, however, is often not unique. In this cases, templates are not always reliable and it is better to infer probability distributions of the coefficients. These can be used as priors when data are available, and can generate tentative templates based on the most probable coefficients. This PCA-based framework for the reconstruction of Cepheid RV curves is useful for investigating the structure and kinematics of the Milky Way and resolved galaxies, as well as for detecting spectroscopic binaries in great numbers and across a variety of environments based on relatively few observations; especially in the future as spectroscopic surveys will increasingly incorporate the temporal dimension into their strategies (Mainieri et al. 2024).

Measuring galaxy kinematics and structure implies that observed samples may substantially differ in metallicity, e.g., due to Galactic abundance gradients (e.g., Luck & Lambert 2011; Genovali et al. 2014) or differences in mean metallicity among Cepheids in the Large and Small Magellanic Clouds (LMC, SMC) (Romaniello et al. 2022; Breuval et al. 2024). Since RVs are measured from absorption lines whose strength varies with chemical composition, it is necessary to investigate the performance of RV templates derived from Galactic Cepheids with roughly Solar metallicity in such cases. Metallicity has been reported to affect light curve shapes (e.g. Klagyivik et al. 2013; Hocdé et al. 2023) and the projection factor for BW analyses (Nardetto et al. 2011). However, studies focused on RVs have reported mixed results: early works found evidence of an increasing amplitude of the RV curves for lower metallicity (Pont et al. 2001; Klagyivik & Szabados 2007; Szabados & Klagyivik 2012), whereas Hocdé et al. (2024) did not find such a correlation and called for further investigation.

This paper is organized as follows. Section 2 describes the data and methodology utilized to determine the templates and evaluate their performance. In Section 3.1, we present the results, discuss precision, limitations and the templates' potential. Section 4 reports the methodology and results of the applications of our templates to literature RV measurements of Cepheids in the LMC and SMC. The final Section 5 summarizes our results and presents our conclusions and perspectives.

2. Data and methods

This work adopted the following nomenclature to distinguish between related, yet conceptually distinct, quantities related to RV analysis. Radial velocities measured from spectroscopic observations are referred to as RV measurements. The intrinsic RV variation of a Cepheid over its pulsation cycle is referred to as its RV curve, and we consider the Fourier series models (VFS), which were determined and carefully checked as part of VELOCE-I, as the corresponding ground truth. Continuous functions used to represent the pulsational RV curve based on the PCs are referred to as \mathcal{M} . Unless otherwise noted, \mathcal{M} is established by fitting PCs to data points drawn from the VFS models. A distinction is made for PC-based models fitted to RV measurements, which are labeled \mathcal{M}_{RV} .

Using this nomenclature, Section 2.1 provides an overview of the data used in this work. Sections 2.2 and 2.3 describe the methodologies adopted. In Section 2.2, we outline the determination of the PCs and the evaluation of their performance over the VELOCE-I sample, while Section 2.3 describes our approach for inferring PC-based priors for use in fitting of sparse time series data.

2.1. VELOCE observations and FS models

VELOCE-I published more than 18000 RV measurements of 258 Galactic classical Cepheids across both hemispheres. Highprecision RV measurements were obtained via the crosscorrelation technique (Baranne et al. 1996), resulting in typical uncertainties ranging from 2 to 50 m s⁻¹. The extensive dataset yields well-sampled pulsation RV curves over a decadelong baselines for most targets, enabling the characterization of the pulsation curve for 219 Cepheids. In VELOCE-I, pulsational variability was modeled using Fourier series (FS), supplemented by a polynomial for cases exhibiting a variable average velocity, e.g., in the case of suspected binaries. Where necessary, we isolated the pulsational variability from the RV measurements by subtracting variations in v_{ν} using these polynomial trends. We adopted the ephemerides from VELOCE-I to ensure consistent alignment of all RV curves. Following Anderson (2016), pulsation phase, ϕ , is defined such that $\phi = 0$ corresponds to minimum radius, i.e., the intersection of the descending branch with v_{γ} . This convention optimizes precision for ϕ and differs from the definition generally used in light curve analyses, where $\phi = 0$ usually refers to maximum light, which typically occurs $\Delta \phi \approx 0.1 - 0.2$ after minimum radius.

2.2. Principal Component Analysis of VELOCE FS models

We applied PCA to finely sampled pulsational RV models of 219 Cepheids constructed by sampling the VELOCE-I Fourier series models on a uniform grid of N_{dim} =1000 points between $0 \le \phi < 1$ (as done, e.g., in RR Lyrae light curves in Hajdu et al. 2018). Since V^{FS} were carefully determined in VELOCE-I,

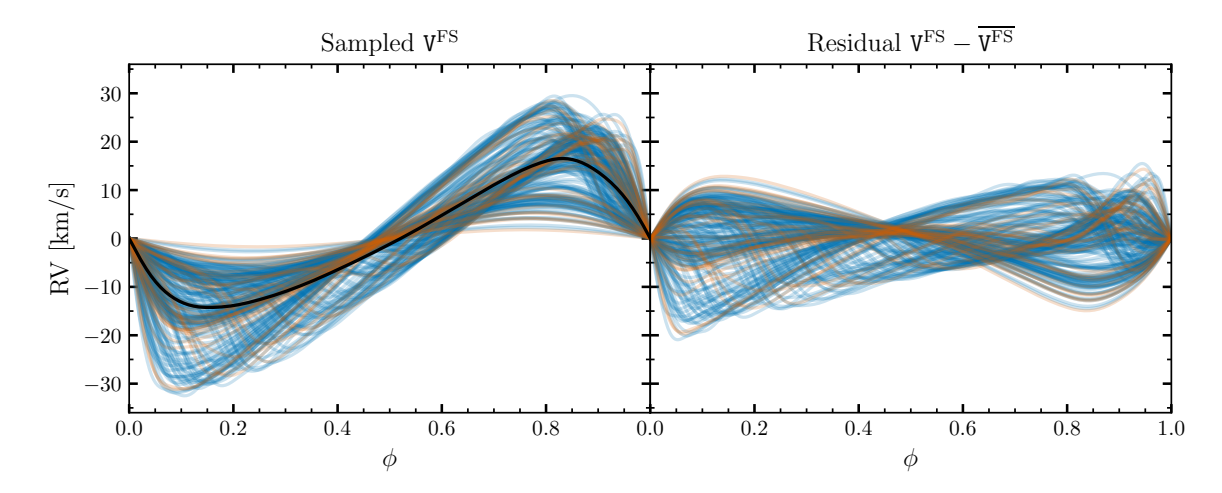


Fig. 1. Cepheids' RV curves published in VELOCE-I. On the left panel, we report the sampled V^{FS} for both the training (blue) and test (orange) set. The solid black line indicates the mean curve of the training set, $\overline{V^{FS}}$. The residual curves after subtracting $\overline{V^{FS}}$ are reported in the second panel.

we considered them a satisfactory approximation to the true RV curve. Moreover, we preferred using discrete model points rather than FS coefficients (e.g., a_n , b_n , ϕ_{n1} , A_{n1}), since the latter would introduce complications related to the different numbers of harmonics fitted for different stars, which depend on the sampling and RV curve complexity. All sampled curves were assigned identical weights for simplicity.

The dataset was divided into training and test sets by randomly setting aside 15% of the targets for testing. After examining several normalization strategies, we decided to remove the mean value of the training V^{FS} at each point of the grid, $\overline{V^{FS}}$, without applying any kind of standardization to the single curves and/or along each dimension (phase bin). This choice ensures that the amplitude information of the curves is maintained in the residuals, $V^{FS} - \overline{V^{FS}}$, and can be captured by the PCs. Figure 1 shows the V^{FS} used before and after this process.

We performed PCA of the training set using the scikit-learn Python library (Pedregosa et al. 2011a) and obtained the individual PCs which relate to the original curves as follows:

$$\nabla^{\text{FS},t}(\phi) = \overline{\nabla^{\text{FS}}}(\phi) + \sum_{i=1}^{N_{dim}} p_i^{\text{FS},t} \, \text{PC}_i(\phi) \,, \tag{1}$$

where $p_i^{\rm FS,t}$ are the projection coefficients for a specific target t. We determined the optimal number of PCs ($N_{\rm PC}$) to retain by analyzing the explained variance, selecting the smallest number of components that capture a sufficiently high fraction of the total variance, thus balancing dimensionality reduction and reconstruction accuracy. Finally, we evaluated the ability of the PCs to reconstruct RV curves based on RV measurements of the test and training sets using v_{γ} , peak-to-peak amplitude (P2P), and the root-mean-square error (RMSE) as quantitative metrics. The results thereof are shown in Sect. 3.2.

2.3. Turning PC coefficients into RV curve fitting priors

We defined priors for use in fitting sparsely sampled RV curves based on the resulting PC coefficients $p_i^{\rm FS}$ ($i=1,...,N_{\rm PC}$). To this end, we first created a two-dimensional mapping of $p_i^{\rm FS}$ vs. $\log P$ by interpolation using two-dimensional multivariate kernel density estimation (KDE) as implemented in the statsmodels

Python library (Seabold & Perktold 2010). Marginalizing the resulting empirical probability distributions at a given value of log *P* thus provides prior probability distributions for fitting RV measurements using the Maximum a Posteriori (MAP) method. MAP is an analog of the more commonly used Maximum Likelihood estimation (MLE) where the distribution has become a posterior (Bassett & Deride 2019), and it can also be interpreted as a regularized form of MLE. Conceptually, MAP estimation refines the parameter estimates by balancing the information from the observed data (as in MLE) with prior knowledge about the parameters. Section 3.3 presents the corresponding results and evaluates the performance of this approach.

We note that we did not create template RV curves in the classical sense; rather, we mapped of $p_i^{\rm FS}$ across $\log P$ as this allows to obtain the most accurate fit to any number of RV measurements using MAP. As a limiting case, classical RV curve templates may be readily constructed by selecting the maximum of each $p_i^{\rm FS}$ at a given $\log P$. The 2D distribution of $p_i^{\rm FS}$ vs $\log P$ is published via the Centre de Données astronomiques de Strasbourg (CDS).

3. Results

This section describes the results of the PCA applied to the V^{FS} models and the determination of prior probability distributions for accurately fitting RV measurements. Section 3.1 presents the retained PCs and corresponding $p_i^{\rm FS}$ coefficients for the sample of Cepheids analyzed. Section 3.2 evaluates the performance of the PCs in terms of reproducing the training and test sets from the RV measurements. Section 3.3 describes the determination of PC priors and evaluates the performance, notably in the context of few available observations.

3.1. Principal Components

We performed PCA and determined the explained varianceratio (EVR) for $1 \le N_{PC} \le 20$ to select the most appropriate N_{PC} for all further analysis. Figure 2 shows the resulting EVR per PC component and demonstrates that most of the variance is captured by the first few components, as seen in PCA of Cepheid light curves (e.g Bras et al. 2025). This behavior persists even when PCA is performed separately on the fundamentalmode and overtone subsamples, indicating no significant mode-

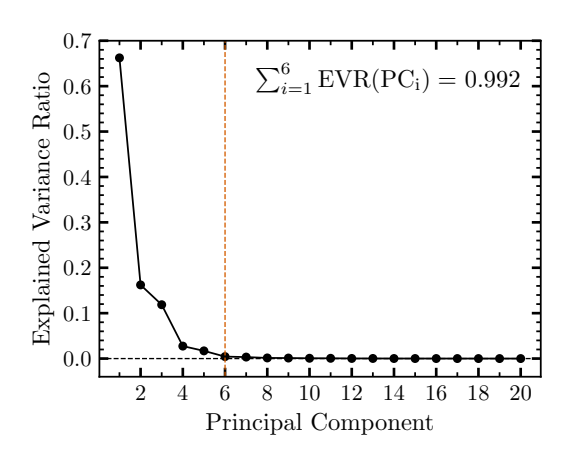


Fig. 2. Variance ratio explained by each PC. The vertical orange dashed line separates the retained (left) and discarded (right) PCs. The total explained variance ratio of the retained PCs is shown in right top corner.

dependent reduction in dimensionality. We therefore chose not to partition the training sample further and retain the first 6 components ($N_{PC}=6$), which cumulatively explain $\sim 99.2\%$ of the total variance. The corresponding PCs are displayed in Fig. A.1.

Using these six PCs, we fitted the V^{FS} models of both training and test sets to obtain the reconstructed models, \mathcal{M} , and their respective coefficients p_i^{FS} . Figure 3 shows the distribution of the coefficients p_i^{FS} against $\log P$. The coefficients for training and test targets follow consistent trends. Interestingly, the PCs bear some resemblance to the distributions of Fourier parameters shown in Fig. 11 of VELOCE-I. PC₁ resembles the inverted distribution of peak-to-peak amplitudes, indicating that the first component primarily accounts for the variability associated with the overall amplitude of the pulsation. The distributions of PC₂ and PC₃ mostly resemble the Fourier amplitude ratios, R_{21} and R_{31} , albeit with some differences and some possible resemblance between PC₂ and the Fourier phase difference ϕ_{21} as well. Higher-order PCs exhibit increasingly less obvious trends, which is also the case among the Fourier amplitude ratios.

The results of the two-dimensional KDE (cf. Sect. 2.3) for each p_i^{FS} against $\log P$ are shown via gray contours in Fig. 3. These distributions capture both the training and test data well without overfitting the empirical points.

3.2. Evaluating PC Performance

We evaluated the performance of the retained PCs by fitting RV measurements from the test and training datasets and comparing our results to the results based on FS models published in VELOCE-I. Specifically, we considered the parameters v_{γ} and P2P, and we computed the RMSE between the fitted PC model, M_{RV} , and V^{FS} , each evaluated at 1000 equidistant values of ϕ . Additionally, we considered each of these parameters in percent of the P2P amplitude of each star as given by V^{FS} , $P2P_{VELOCE}$, since amplitudes exhibit a strong dependence on $\log P$ and pulsation mode. Distinguishing between test and training sets allowed us to evaluate whether the PCs generalizes well to unseen data and/or identify potential discrepancies that would indicate either over-fitting, an unfavorable dataset split, or other limitations of the analysis. Figure 4 illustrates these results.

We identified six Cepheids as outliers: AV Sgr, BB Gem, IR Cep, α UMi (Polaris), V0440 Per, and

ASAS J064540+0330.4. AV Sgr was excluded from further analysis, since the few number of measurements, $N_{RV} = 9$, were all located on the ascending branch of the pulsation, thereby poorly constraining any RV curve fits. In the cases of BB Gem and IR Cep, the sparsely sampled maximum of the RV curve and the complex structure of the data, respectively, yielded fitted PC models that deviated from the corresponding FS models. Since both solutions reproduce the RV measurements comparably well, and no objective criterion could favor one over the other, these stars were retained in the analysis. The outlier nature of the remaining three stars, α UMi, V0440 Per and ASAS J064540+0330.4, is explained by their unusually low amplitudes for their respective $\log P$, which were not sufficiently represented in the training data. Since such issues may also arise when applying our framework to other stars with abnormally low amplitudes, we retained these targets in our analysis.

3.2.1. $\Delta v_{\gamma} = v_{\gamma} - v_{\gamma, \text{VELOCE}}$

As shown in Fig. 4a, we found a strong agreement between the $M_{\rm RV}$ and V^{FS} models. The scatter in Δv_{γ} is balanced around 0 across $\log P$, with average $11~{\rm m\,s^{-1}}$ and standard deviation of $73~{\rm m\,s^{-1}}$. The training and test samples show consistent results with mean (standard deviation) values of $8~{\rm m\,s^{-1}}$ ($75~{\rm m\,s^{-1}}$) and $28~{\rm m\,s^{-1}}$ ($55~{\rm m\,s^{-1}}$), respectively, indicating that the obtained PCs generalize well. As mentioned above, BB Gem and IR Cep appear as outliers for $\log P < 0.4$. The large error for BM Per is explained by an uneven sampling of RV measurements mostly located on the ascending branch of the RV curve, similar to AV Sgr.

The ratio $\Delta v_{\gamma}/P2P_{\rm VELOCE}$, which removes the large differences in amplitude among stars, is shown in Fig. 4b. For 90% of the targets, v_{γ} is recovered within 0.32% of $P2P_{\rm VELOCE}$. The scatter is particularly small for $\log P > 1$, and overall appears to decrease with $\log P$, and thus generally the amplitude.

3.2.2. $\Delta P2P = P2P - P2P_{\text{VELOCE}}$

Figure 4c illustrates the results for $\Delta P2P$ and Fig. 4d the corresponding relative differences. In 90% of all cases, we found P2P within $\sim 1.6 \,\mathrm{km \, s^{-1}}$ of the expected result; 90% of amplitudes are recovered to within 4.2% of the expected values. As mentioned before, stars with abnormally low amplitudes (α UMi, V0440 Per and ASAS J064540+0330.4) appear as clear outliers. The two figures clearly reveal a tendency to systematically underestimate amplitudes between 9.7 < P[d] < 20. Below $P \sim 9.7 \text{d} (\log P \sim 0.987)$, both $\Delta P2P$ and $\Delta P2P/P2P_{\text{VELOCE}}$ are symmetrically well-balanced around 0, and their scatter remains narrow and nearly constant, with 90% of the values within merely 0.8 km s⁻¹. At longer periods, the fact that the HP is not a unique function of $\log P(\text{cf. Figs. }11 \text{ and }12 \text{ in VELOCE-I})$ introduces an astrophysical limitation to how closely RV curve shapes can be generalized. As a result, P2P is typically somewhat underestimated for $\log P \in [1, 1.3]$ and slightly overestimated at $\log P > 1.3$. The systematics under- and overestimation thus arise from the diversity of RV curves across the Hertzsprung progression (HP), where (double) bump features appear near the minimum ($\log P$ 1) and maximum ($\log P > 1.3$) of the RV curve. For very long-period Cepheids, further limitations include the lower density of stars (in log P) and the difficulty of achieving sufficiently good phase coverage for stars exhibiting significant cycle-to-cycle variations and complex period changes (Anderson 2014; Csörnyei et al. 2022, VELOCE-I).

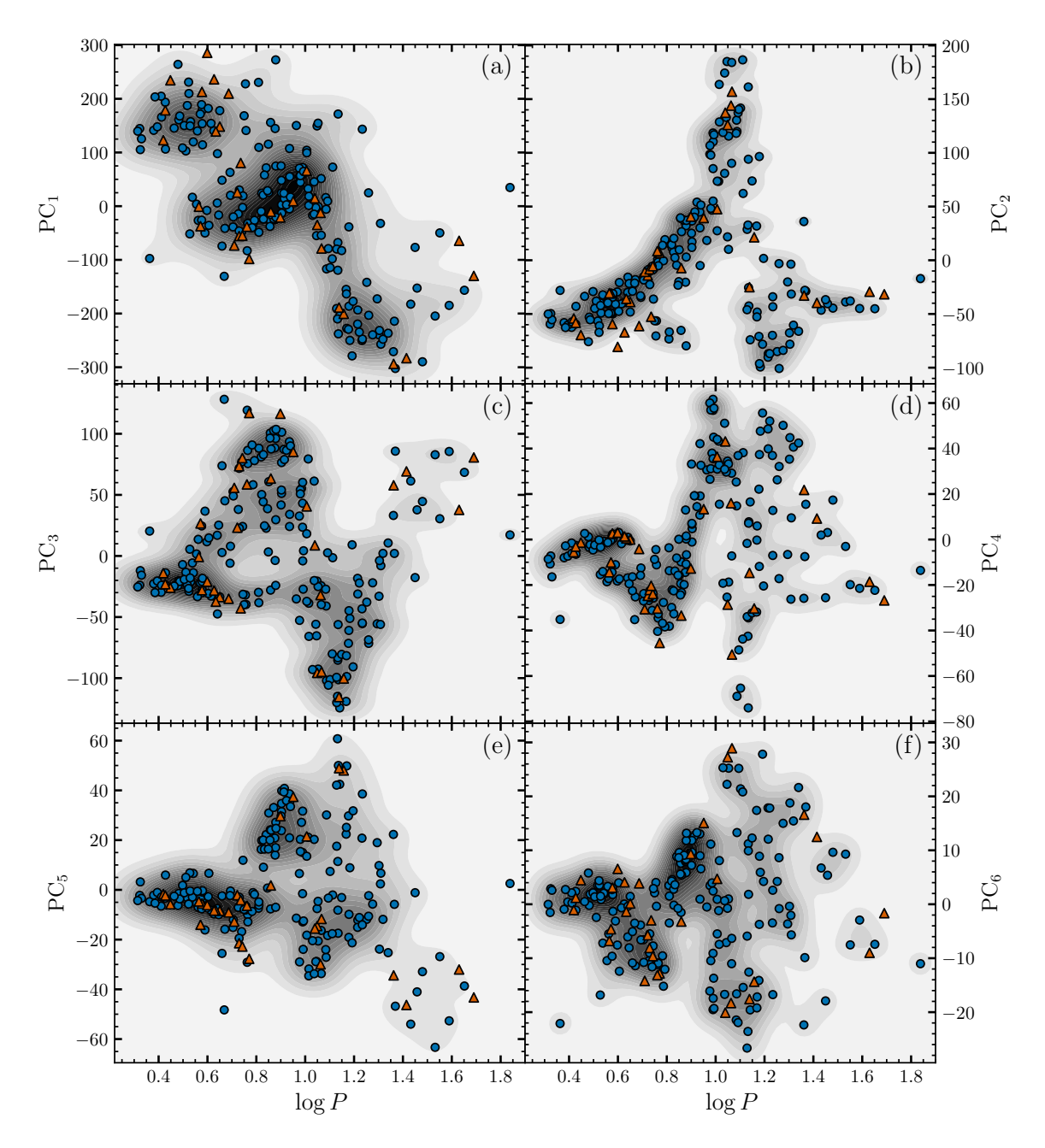


Fig. 3. Distribution of the coefficients p_i^{FS} of the \mathcal{M} models as a function of the logarithm of the pulsation period, $\log P$. As for the previous plots, the training set is presented in blue, whereas the test set in orange. In the background, the KDE distributions obtained from the training set are shown in grayscale.

3.2.3. *RMSE*

The *RMS E* computed between M_{RV} and V^{FS} quantifies the average difference between the two models in km s⁻¹. Figures 4e and 4f show the *RMS E* in km s⁻¹ and as a percentage of $P2P_{VELOCE}$, respectively. Overall, these distributions confirm the strong performance of the PCs in accurately reconstructing the V^{FS} curves from the RV measurements. The mean RMSE and its scatter both increase with the pulsation period. For most Cepheids with $\log P < 0.8$, RMSE remains below $0.3 \, \mathrm{km \, s^{-1}}$, while for longer period stars, which are characterized by the HP bump, the threshold rises to $\sim 1 \, \mathrm{km \, s^{-1}}$. The 90% percentile of the distributions is found at $0.848 \, \mathrm{km \, s^{-1}}$, and at $\sim 2.3\%$ of the total pulsation amplitude. The relative RMSE distribution in Fig. 4f shows a weaker

dependence on the pulsation period, yet confirms the inability of the PCs to reliably reproduce the HP bump for Cepheids within $\log P \in [1, 1.3]$. The envelope of lowest relative *RMS E* in Fig. 4f also exhibits a clear trend with $\log P$. As expected, all 5 discussed outliers exhibit larger *RMS E* values than the rest of the targets.

3.3. RV curve fits based on PCs with Priors

A key application of the PCs calibrated in this work lies in the determination of RV curves from sparsely sampled time series, with the particular emphasis on accurately estimating ν_{γ} in order to investigate stellar multiplicity and galaxy kinematics. To test the performance of our methodology, we here

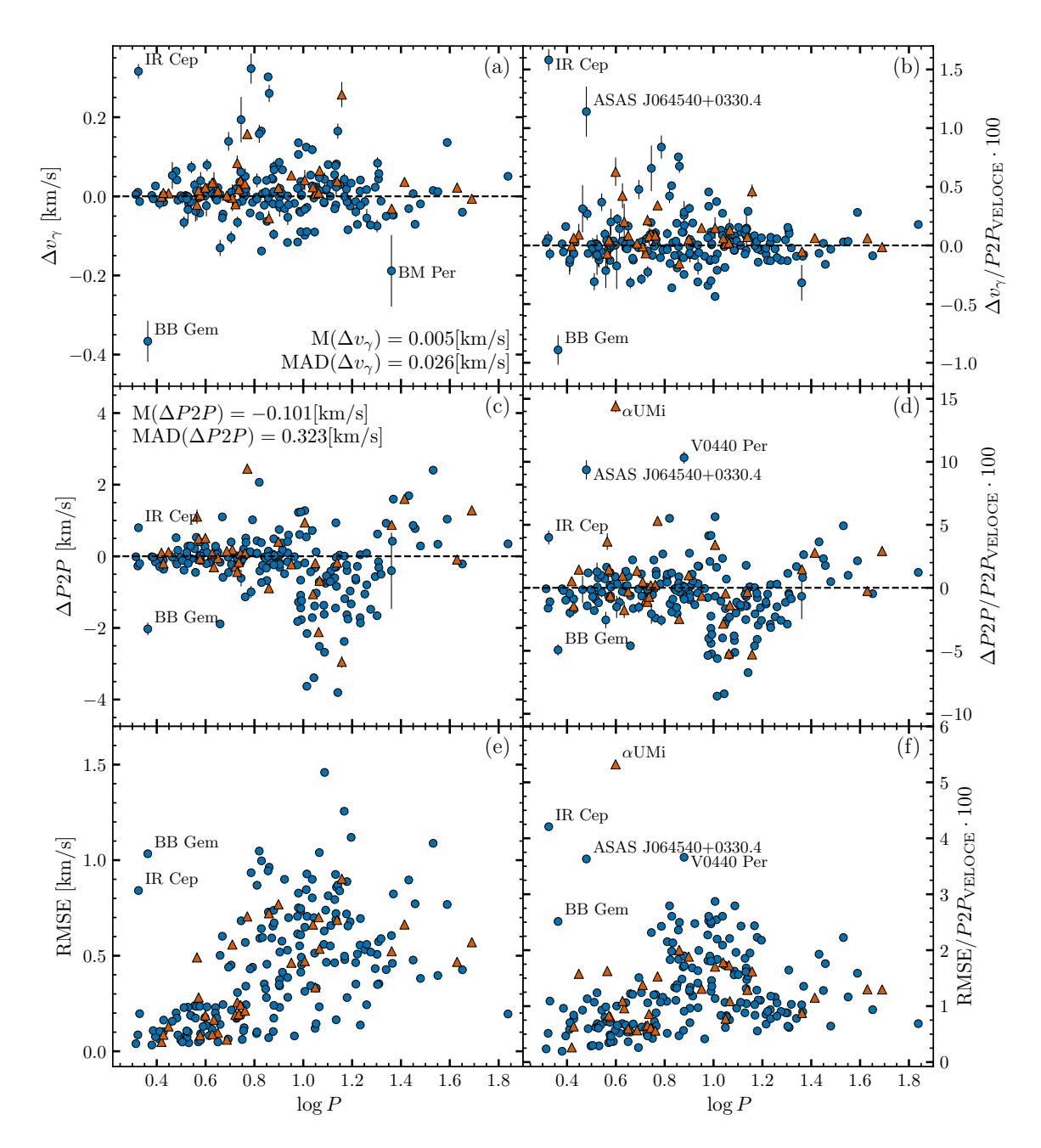


Fig. 4. Performance of the obtained PCs when fitting VELOCE-I data. The training and test set members are colored in blue and orange respectively. The left panels from top to bottom: the difference in pulsation average velocity, Δv_{γ} , the difference in peak-to-peak amplitude, $\Delta P2P$, and *RMS E*. The right panels present the same quantities as percentage of the target's $P2P_{\text{VELOCE}}$.

applied the MAP method to the marginalized prior distributions (cf. Section 2.3) while varying the number of RV measurements, $N_{\rm RV} \in [3, 4, 5, 6, 7, 10, 15, 20]$. For each Cepheid, we randomly selected $N_{\rm RV}$ measurements (without replacement) from VELOCE-I and fitted the RV curve using the MAP method and our priors. As initial estimates for the PCs coefficients, we adopted the maxima of the prior distributions, thereby emulating the case of an uncharacterized target. The additive velocity offset was initialized as the mean residual between the observed RVs and the pulsation signal reconstructed from this initial estimate. The procedure was repeated 100 times, each using a unique random subset, in order to characterize the distribution of possible fits mitigating sampling variability. We computed mean and standard deviation for each of these distributions and analyzed

how the precision and accuracy evolve as a function of $N_{\rm RV}$. To minimize correlation among subsamples, targets with fewer than $\leq N_{\rm RV} + 2$ available measurements were excluded; the only exception was V1197 Cen (9 observations), for which we utilized the 84 distinct combinations available for $N_{\rm RV} = 3$ and 6.

Figure 5 presents the results for the sparsest samples considered with $N_{\rm RV}=3$. Some iterations yielded poor fits due to inadequate phase sampling. We intentionally kept these cases in order to maintain realism, since large surveys tend to observe objects at random phases. The reported standard deviations thus reflect such suboptimal cases.

To summarize the results as a function of $N_{\rm RV}$, we estimated the central tendency and dispersion for Δv_{γ} , $\Delta P2P$, and the ratio $\Delta P2P/P2P_{\rm VELOCE}$ from each distribution by bootstrap resam-

Table 1. Recovery of RV curve properties from few observations

$\overline{N_{ m RV}}$	$N_{targets}$	$M(\Delta v_{\gamma})$ [km s ⁻¹]	$M(\Delta P2P)$ [km s ⁻¹]	$M(\Delta P2P/P2P_{\text{VELOCE}})$ [%]	$P_{90}(RMSE)$ [km s ⁻¹]	$P_{90}(RMSE/P2P_{VELOCE})$ [%]
3	218	-0.008 ± 0.314	-0.176 ± 2.140	-0.65 ± 6.75	3.615	12.09 (10.06)
4	218	-0.013 ± 0.344	-0.116 ± 1.854	-0.41 ± 5.92	3.025	9.96 (8.71)
5	218	-0.012 ± 0.362	-0.040 ± 1.718	-0.15 ± 5.50	2.638	8.86 (7.67)
6	218	-0.009 ± 0.350	0.048 ± 1.592	0.18 ± 5.13	2.470	7.61 (6.75)
7	217	-0.011 ± 0.342	0.103 ± 1.514	0.39 ± 4.91	2.312	6.78 (6.44)
10	215	-0.002 ± 0.263	0.068 ± 1.165	0.25 ± 3.76	1.855	5.12 (4.96)
15	206	0.004 ± 0.142	-0.006 ± 0.719	-0.02 ± 2.36	1.370	3.72 (3.67)
20	191	0.004 ± 0.093	-0.041 ± 0.558	-0.16 ± 1.83	1.133	3.07 (3.05)

Notes. Summary of the application of the PCs and priors to subsamples of the available RV measurements. N_{RV} denotes the number of RV measurements per target, and $N_{targets}$ the total number of targets analyzed. $M(\Delta v_{\gamma})$, $M(\Delta P2P)$ and $M(\Delta P2P/P2P*100)$ list the median and MAD values obtained via bootstrap resampling for the corresponding quantities. $P_{90}(RMSE)$ and $P_{90}(RMSE/P2P_{\text{VELOCE}})$ give the 90th-percentiles of the RMSE and of its ratio over the peak-to-peak amplitude. For the latter, values computed after excluding the identified outliers are given in parenthesis.

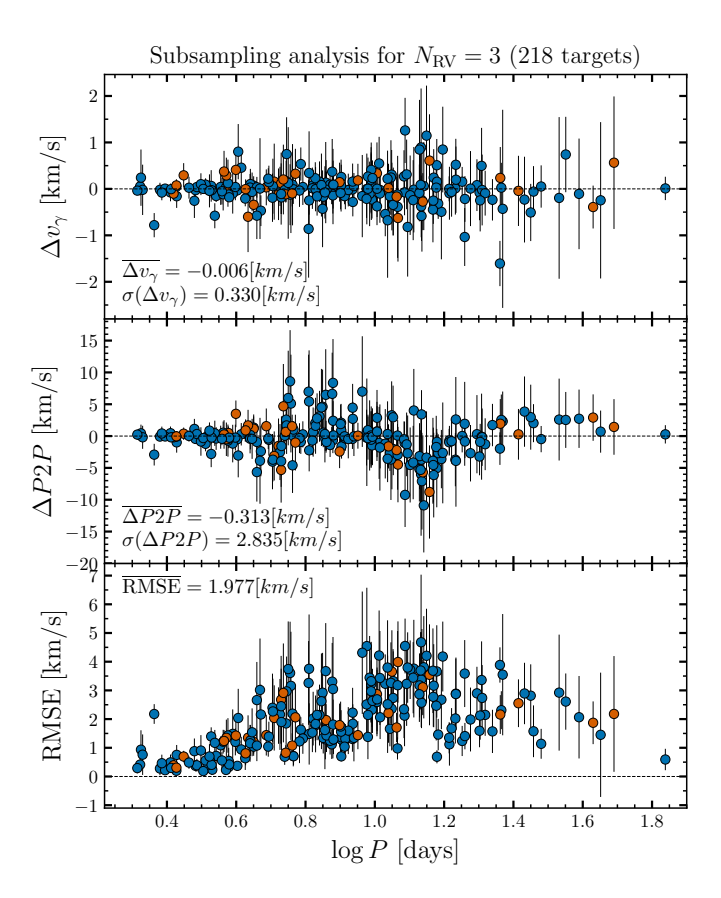


Fig. 5. Performance of the PCs and priors applied to subsamples of size $N_{\rm RV}=3$. Each panel shows each target's mean and standard deviation of the results obtained for all combination. From top to bottom, the statistics reported are: Δv_{γ} , $\Delta P2P$ and RMSE.

pling. For each target, we modeled the measured mean and standard deviation as Gaussian distributions from which new synthetic datasets were drawn for each bootstrap realization. For each realization, we computed the median, M, and median absolute deviation, MAD. We repeated this process 10^4 times, and the medians of the median and MAD distributions were adopted as final estimates. The resulting values are reported in Tab. 1, and illustrated in Fig. 6. The choice of using the median and MAD mitigates the impact of the outliers and sample-specific fluctuations, providing a more robust assessment of the effectiveness

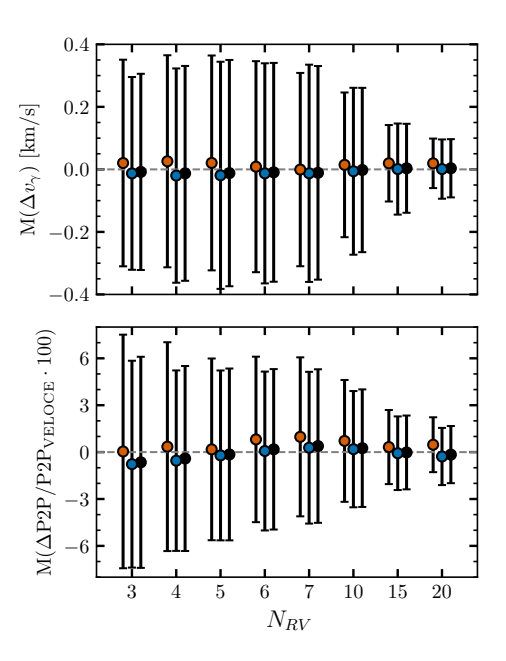


Fig. 6. Accuracy of v_{γ} (top) and P2P (bottom) from MAP fitting as a function of the number of available observations, $N_{\rm RV}$. Median and MAD values obtained via bootstrap (see Section 3.3) are shown for the training (blue) and test (orange) sets, and their union(black).

of this methodology to accurately reconstruct the RV curve as a function of $N_{\rm RV}$.

3.3.1.
$$\Delta v_{\gamma} = v_{\gamma} - v_{\gamma, \text{VELOCE}}$$

The pulsation average velocity, v_{γ} , is accurately recovered for all targets, even when only 3 observations are available. The top panel of Fig. 5 reveals no bias, and the scatter of Δv_{γ} is well contained within the uncertainties: 197 out of 218 targets (90%) fall within 1- σ , 214 (98%) within 2- σ , and 98.5% of the mean values lie within 1 km s⁻¹ of the reference $v_{\gamma, \text{VELOCE}}$. These results suggest that the estimated σ values slightly overestimate the underlying true scatter, as they also account for the results of the few suboptimal cases.

The results as a function of $N_{\rm RV}$ reveal excellent performance for both test and training datasets. As listed in Tab. 1 and shown in Fig. 6a, $MAD(\Delta v_{\gamma}) \approx 350\,{\rm m\,s^{-1}}$ for $N_{\rm RV} \leq 7$ and improves

for larger $N_{\rm RV}$. The consistency between training and test sets improves by a few tens of m s⁻¹ when more than three observations are available. Hence, we find that our framework can in principle determine v_{γ} to within $\pm 0.35~{\rm km~s^{-1}}$ without bias at the level of the typical precision level of per-epoch VELOCE-I measurements using merely three observations. Applications requiring precision better than $0.2~{\rm km~s^{-1}}$ ($0.1~{\rm km~s^{-1}}$) on v_{γ} require larger $N_{\rm RV} \sim 12$ (20).

3.3.2. $\Delta P2P = P2P - P2P_{VELOCE}$

The recovery of P2P reveals generally good performance with no globally apparent bias. However, as mentioned in Sect. 3.2.2, the reproduction of peak-to-peak amplitudes is hampered by the complexities inherent to the HP, notably for $\log P \in [1, 1.3]$. We found the same tendencies in $\Delta P2P$, cf. Fig. 5 for $N_{\rm RV}=3$ as those shown in the fits based on the full data set in Fig. 4. This consistency confirms that the priors effectively constrain the fitted PC coefficients towards the values one would obtained with full information (i.e. all RV measurements), even for very sparse sampling.

The recovery of P2P depends more strongly on $N_{\rm RV}$ than v_{γ} does. Both panels of Fig. 6 show similar trends, albeit $M(\Delta P2P/P2P_{\rm VELOCE})$ exhibit more noticeable improvements at low $N_{\rm RV}$. For $N_{\rm RV}=3$, $MAD(\Delta P2P/P2P_{\rm VELOCE})\sim 6.75\%$, and 90% of amplitudes were recovered within $\sim 15\%$ of the reference value. For all $N_{\rm RV}\geq 3$, the agreement between test and training set is at the 1% level or better and the P2P values of the full sample are unbiased at the same level. Improving precision to better than 4% (2%) requires $N_{\rm RV}>10$ (20).

3.3.3. *RMSE*

The overall agreement in the PC-based fit and the VELOCE FS fit as measured by RMSE was found to depend both on $N_{\rm RV}$ and on $\log P$, likely due to the correlated trend of P2P. RV curves for $\log P < 0.6$ are mostly reproduced to within $< 1~{\rm km\,s^{-1}}$ or better even for $N_{\rm RV} = 3$. Globally, the agreement in RMSE expressed for 90% of Cepheids improved from $\sim 3.6~{\rm km\,s^{-1}}$ to $\sim 2.3~{\rm km\,s^{-1}}$, and $\sim 1.1~{\rm km\,s^{-1}}$ for $N_{\rm RV} = 3$, 7, and 20, respectively. Analogously, the 90th percentile of $RMSE/P2P_{\rm VELOCE}$ improved from 12% to 7%, and to 3%.

Interestingly, the $RMSE/P2P_{VELOCE}$ distribution revealed a group of seven clear outliers whose values exceeded 20% for $N_{\rm RV}=3$: V0440 Per, MY Pup, α UMi, ASAS J184741-0654.4, V0659 Cen, ASAS J084412-3528.4, and HW Car. All of these stars have unusually low P2P (to varying degrees) compared to most Cepheids with similar log P. The cases of V0440 Per and α UMi were already discussed in Sect. 3.1, and their RMSE/P2P_{VELOCE} values remain elevated regardless of N_{RV} , indicating that such stars were not sufficiently present in the training data as a consequence of their rarity (ASAS J064540+0330.4, show a more moderate ratio of 15.9%). For the remaining four stars, satisfactory fits are obtained for $N_{\rm RV} \geq 7$, where the phase coverage is usually sufficient to constrain atypical low-amplitude RV curve. The last column of Tab. 1 reports, in parentheses, the values computed after excluding these seven outliers, highlighting their disproportionate influence on the overall sample, particularly for $N_{\rm RV}$ < 10. We further note that all of these Cepheids, aside from HW Car, exhibit modulated RV curves, cf. Tab. 3 of VELOCE-I.

4. Application to extragalactic Cepheids

We applied our framework to time-series RV measurements of Cepheids in the LMC and SMC (cf. Sect. 4.1) in order to test its performance at a metallicity systematically lower than the VELOCE-I data set, which is mostly comprised of near Solar metallicity Cepheids (cf. Fig. 20 in VELOCE-I, which implies an average near +0.1 with considerable scatter), whereas the mean metallicity of SMC and LMC Cepheids is lower, [Fe/H]_{LMC} = -0.409 \pm 0.076 (Romaniello et al. 2022) and [Fe/H]_{SMC} = -0.785 \pm 0.082 (Breuval et al. 2024, citing Romaniello et al. in prep.). Additionally, we modified our methodology to specifically search for spectroscopic binaries (Sect. 4.2), and sought to obtain a first view of the line-of-sight velocity distributions of both Clouds. The results for the LMC and SMC are presented in Sects. 4.3 and 4.4, respectively.

4.1. Literature RVs of extragalactic Cepheids

Storm et al. (2011) published 509 precise RV measurements (per-epoch uncertainty ≤ 100 m s⁻¹) of 22 fundamental mode Cepheids in the Large Magellanic Cloud (LMC) based on observations with HARPS (Mayor et al. 2003) and FEROS (Kaufer et al. 1999) (used only for HV914 and HV12717). Most spectra were collected during a single 16-nights observing run, with additional epochs obtained over the following two seasons to fill phase gaps. While this strategy yielded densely sampled RV curves, the relative short temporal baseline limits the detection of possible orbital motion. Indeed, Storm et al. (2011) identified evidence of orbital motion only for HV 1005, where two observations taken two years after the main campaign appear to be shifted from the rest of the RV curve.

As a second dataset, we adopted the RV measurements published by Gieren et al. (2018) for Cepheids in the Small Magellanic Cloud (SMC). This sample comprises 714 RV measurements of 26 Cepheids obtained using 3 high resolution spectrographs: HARPS, MIKE (Bernstein et al. 2003) and UVES (Dekker et al. 2000). These RV measurements have typical perepoch uncertainties of $\sim 250\,\mathrm{m\,s^{-1}}$ and were collected between 2012 and 2017, providing observational baselines sufficient to detect long-term orbital trends. Gieren et al. (2018) included 5 additional targets from Storm et al. (2004) and HV 837 from Imbert et al. (1989). We did not consider these stars here, restricting our analysis to the newly acquired data.

Gieren et al. (2018) reported velocity variations indicative of orbital motion in six of the 26 Cepheids: OGLE SMC-CEP-1680, -1686, -1693, -1729, 1977, and -2905. Among these, SMC-CEP-1686 and SMC-CEP-1693 exhibited particularly complex behavior that prevented the identification of a consistent systemic velocity. In the case of SMC-CEP-1686, concurring with the authors, we noted that the RV variations cannot be described by simple additive offsets, whereas for SMC-CEP-1693, the variations are so large relative to the pulsational amplitude that no sensible RV curve can be identified. While Gieren et al. (2018) analyzed SMC-CEP-1686 without adopting any correction and excluded SMC-CEP-1693 from their analysis, we opted to remove both stars. For the remaining 4 potential binaries, Gieren et al. (2018) minimized the effect of orbital motion by applying epoch-dependent velocity offsets to corresponding data.

4.2. Time-resolved hierarchical fitting and detection of orbital motion

To identify spectroscopic binaries (SB) among the two datasets, we partitioned each RV time series into temporal clusters following the approach of Anderson et al. (2016a, and Sect. 5.1 in VELOCE-I). This procedure enables the determination the pulsation-averaged RV for each cluster, and allows the assessment of its temporal variability, thus retaining sensitivity to orbital motion on longer timescales. As done in VELOCE-I, clustering was performed using KDE with the bandwidth parameter defined as $\max(80, \min(3 \cdot P, 100))d$. Each case was visually inspected, and the bandwidth and/or number of clusters were adjusted to ensure adequate grouping and a minimum of 2 RV measurements per cluster.

We fitted 2 models to the RV measurements. The first, $\mathcal{M}_{\text{RV}}^{\text{SOLO}}$, assumes no orbital motion and fits only the pulsation component as defined by Eq.1. The second, $\mathcal{M}_{\text{RV}}^{\text{MULTI}}$, accounts for possible orbital motion, by fitting a hierarchical model that includes both the pulsational component and cluster-specific pulsation average velocity, $v_{\gamma,\text{cluster}}$. This formulation enables the quantification of variations in the mean velocity over time. Importantly, the pulsation model is shared across all clusters, ensuring that the full dataset contributes to constraining the PC coefficients. For both models, we fitted one additional parameter, $\Delta\phi$, to ensure $\phi=0$ occurs at minimum radius (see Sect. 2.1).

As in Section 3.3, the pulsation component was constrained using the previously derived priors. However, given the high dimensionality and potential parameter degeneracies, we performed the optimization in two steps. First, a global search using the Differential Evolution (DE) algorithm located the best-fit region of the parameter space. Second, a Markov Chain Monte Carlo (MCMC) exploration refined the parameter estimates and characterized their posterior distributions. This strategy provided robust constraints on both the pulsation curve and $v_{\gamma, \text{cluster}}$.

Binaries can be detected when the scatter of individual $v_{\gamma,\text{cluster}}$ measurements significantly exceeds the precision of the $v_{\gamma,\text{cluster}}$ measurements, σ_{cluster} , which is not known a priori, since it depends both on the quality of the RV measurements and the ability to determine v_{γ} with our PC framework. Moreover, the measured dispersion of the $v_{\gamma,\text{cluster}}$ measurements exceeds σ_{cluster} due to the presence of binaries. We therefore determined the typical precision, σ_{cluster} , as the dispersion of the samples after removing the $E[N_{\text{SB1}}]$ objects with the largest scatter, where $E[N_{\text{SB1}}]$ is the expected number of SB1s in the sample.

We determined $E[N_{SB1}]$ from the properties of the orbital solutions determined in VELOCE-II and the temporal sampling of the LMC and SMC datasets, taking into account also the precision of the fitting methodology. We adopted the average RMSEof the \mathcal{M}_{RV}^{MULTI} fits, $\overline{RMSE}(\mathcal{M}_{RV}^{MULTI})$, as a representative measure of the overall precision of the PCs-based models. First, we sampled each VELOCE-II orbit at the mean BJD of each cluster for a randomized orbital phase and added Gaussian noise with a standard deviation of $\overline{RMSE}(\mathcal{M}_{RV}^{MULTI})$, scaled by the square root of the number of observations per cluster. Orbital motion was deemed "detected" if the simulated cluster-to-cluster P2P variation exceeded twice the $RMSE(\mathcal{M}_{RV}^{MULTI})$. We repeated this process a 1000 times to estimate the detection efficiency for each VELOCE-II orbit. The median of the detection efficiency across all VELOCE-II orbital solutions was adopted as the representative detection efficiency for the temporal configuration of the dataset. To quantify the false-alarm probability (FAP) due to noise alone, we repeated the procedure using a constant (non-orbital) RV function. Second, we considered the RV trends reported in Tab. 5

of VELOCE-II and qualitatively estimated which of them could be recovered given the dataset average observational baseline and $\overline{RMSE}(\mathcal{M}_{RV}^{MULTI})$. Lastly, we considered SB1s in VELOCE-II detected solely via the RV Template Fitting (RVTF) unidentifiable within the LMC and SMC datasets because of their rather short temporal baselines. The typical precision, $\sigma_{cluster}$, was thus computed based on the sample of Cepheids reduced by the E[SB1] exhibiting the largest variations in $v_{\gamma,cluster}$:

$$\sigma_{\text{cluster}} = \sqrt{\frac{\sum_{i} \sum_{\text{cluster}} (\nu_{\gamma, \text{cluster}, i} - \overline{\nu_{\gamma, \text{cluster}, i}})^{2}}{N_{\text{clusters}, \text{No SB1}}}}$$
(2)

where $N_{\text{cepheids,No SB1}} = N_{\text{Cepheids}} - E[N_{\text{SB1}}]$, $N_{\text{clusters,No SB1}}$ is the total number of temporal cluster for the $N_{\text{cepheids,No SB1}}$ targets, and $\overline{v_{\gamma,\text{cluster,i}}}$ the mean velocity of all clusters for the *i*th Cepheid.

Finally, we considered SB1 candidates any Cepheids with at least one $3\sigma_{\text{cluster}}$ outlier cluster measurement, i.e., where:

$$f_{\sigma,\text{cluster}} = \max(|v_{\gamma,\text{cluster}} - \overline{v_{\gamma,\text{cluster}}}|)/\sigma_{\text{cluster}} \ge 3$$
. (3)

The following reports the results from the \mathcal{M}^{SOLO}_{RV} model for stars where no orbital motion was detected; for candidate SB1s, the results from the \mathcal{M}^{MULTI}_{RV} analysis are presented.

4.3. LMC

Since most of the observations from Storm et al. (2011) were collected during a single observing run, only 12 of the 22 LMC Cepheids yielded more than one temporal cluster. Furthermore, the limited baseline prevented an adequate application our methodology to estimate $E[N_{\rm SB1}]$ and thus $\sigma_{\rm cluster}$ for this dataset.

We fitted the \mathcal{M}_{RV}^{SOLO} model to all targets and the \mathcal{M}_{RV}^{MULTI} model to the 12 targets with multiple clusters. The fit for HV877 indicated that the measurement at BJD $\simeq 54046.71$ is a potential outlier, which we excluded from the analysis.

Figure 8 shows the fitted PC coefficients for each LMC Cepheid in yellow; their distribution closely follows the priors without any significant outliers. Visual inspection of the fitted RV curves revealed overall good agreement, with median $RMSE = 0.79 \, \mathrm{km \, s^{-1}}$ for the simpler \mathcal{M}_{RV}^{SOLO} model.

The \mathcal{M}_{RV}^{MULTI} model yielded substantially better results than the \mathcal{M}_{RV}^{SOLO} model only for HV914, HV1005, and U1 (OGLE LMC-CEP-79); their RMSE decreasing from 1.84 to 1.05 km s⁻¹ for HV914, from 2.84 to 0.83 km s⁻¹ for HV1005, and from 1.86 to 0.59 km s⁻¹ for U1. As the panels in Fig. 7 illustrate, the detection of orbital motion appears robust for HV914 and U1. For HV1005, we confirmed the findings of Storm et al. (2011), as two observations collected years after the main campaign are vertically offset from the rest. While this may be indicative of orbital motion, more observations are required to exclude other potential causes, such as phase shifts.

clude other potential causes, such as phase shifts. Adopting the \mathcal{M}_{RV}^{MULTI} fit for these 3 targets and the \mathcal{M}_{RV}^{SOLO} for all others, we found median and 90th percentile of the RMSE to be $0.78\,\mathrm{km\,s^{-1}}$ and $1.16\,\mathrm{km\,s^{-1}}$, respectively, fully consistent with the expected performance and capabilities of the PCs (see Fig. 4e and Tab. 1 for $N_{RV} \geq 15$). The complete set of results is provided in Tab. C.1.

4.4. SMC

Sufficiently long baselines to allow clustering of the observations were available for all 24 Cepheids under analysis. We fitted both \mathcal{M}_{RV}^{SOLO} and \mathcal{M}_{RV}^{MULTI} models to all objects, obtaining

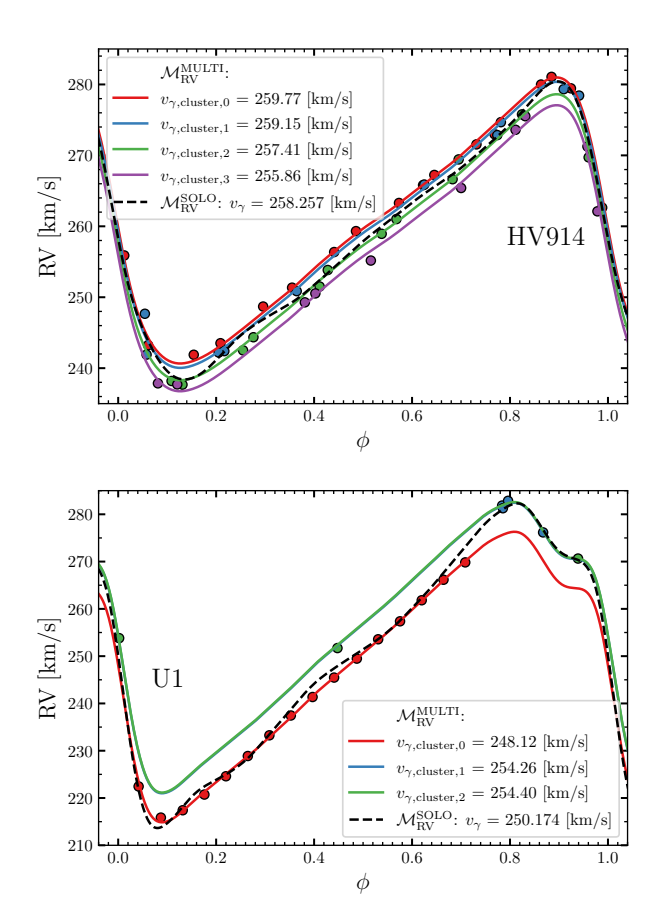


Fig. 7. RV measurements and model fits for HV 914 (top) and U1 (bottom). The data points are color-coded by temporal cluster, with corresponding \mathcal{M}_{RV}^{MULTI} cluster models shown in matching colors. The overall single-epoch fit, \mathcal{M}_{RV}^{SOLO} , is displayed for comparison..

a $\overline{RMSE}(\mathcal{M}_{RV}^{MULTI})=1.21\,\mathrm{km\,s^{-1}}$. The results are tabulated in Tab. C.1 and the fitted coefficients are shown in green in Fig. 8. As for the LMC's Cepheids, the coefficient distributions globally follow the priors, albeit with some differences at the longest and shortest periods, especially for PC₁ and PC₅. The outlier in PC₅ corresponds to SMC-CEP-1729 (log $P\sim0.6$); however, visual inspection confirmed that the obtained fit provides a reasonable reproduction of the RV curve.

After performing VELOCE-II's orbital solutions sampling simulation and estimating its false alarm rate, we determined that roughly $\sim 87\%$ of the 33 VELOCE-II orbits would be detected given the current temporal sampling. For the long term RV trends reported in VELOCE-II, we concluded that between 9 and 12 of those cases could also be recovered. Combining these results yields an expected number of detectable binaries within the Gieren et al. (2018) sample is $E[N_{\rm SB1}](0.87 \cdot 33 + 12(9))/N_{\rm Cepheids}^{\rm VELOCE} \simeq 3.8(3.5) \sim 4.$

Figure 9 illustrates $v_{\gamma, {\rm cluster}}$ as a function of time for the SMC sample. The 4 targets exhibiting with largest $v_{\gamma, {\rm cluster}}$ scatter are: SMC-CEP-1680, -1729,-1977, and -4017. We computed the scatter of the cluster-averaged velocities, $v_{\gamma, {\rm cluster}} - \overline{v_{\gamma, {\rm cluster}}}$, excluding these 4 targets from the calculation and applying Eq. 2, obtaining $\sigma_{\rm cluster} = 0.85 \, {\rm km \, s^{-1}}$.

In total, 6 Cepheids exhibit $v_{\gamma,\text{cluster}}$ scatter exceeding of $3\sigma_{\text{cluster}}$: SMC-CEP-1680, -1729, -1977, -4017, -2905, and -0524. Gieren et al. (2018) previously identified SMC-CEP-1680, -1729, -1977, and -2905, as SB1 Cepheids, and our methodology

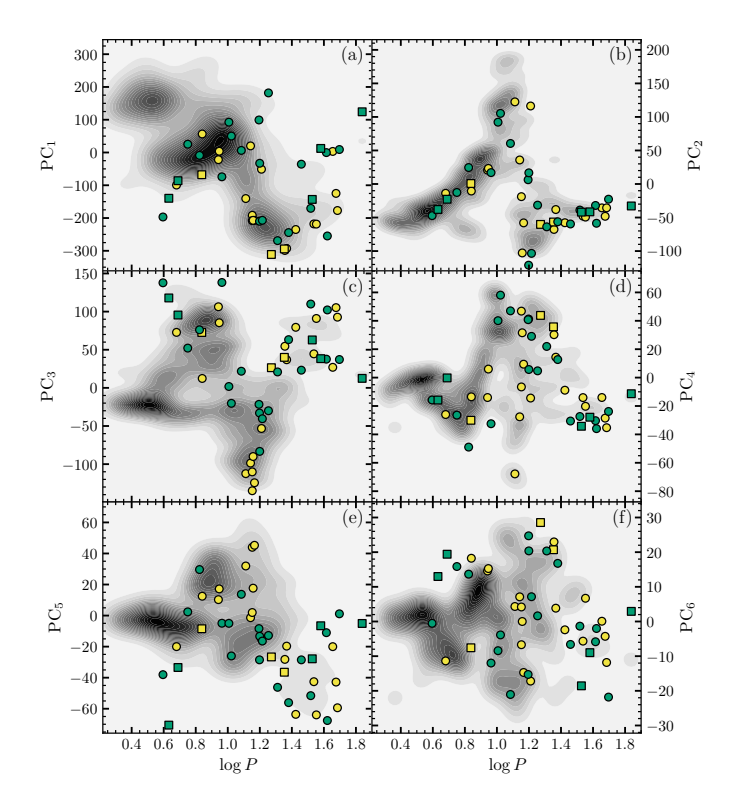


Fig. 8. Distribution of the fitted coefficients for the LMC (in yellow) and SMC (in green) targets plotted over the prior distribution determined in Section 3.3. Determined and suspected binaries are presented as filled squares, whereas the rest are plotted as filled circles.

confirms their result. Following visual inspection of the \mathcal{M}_{RV}^{MULTI} , we concluded that SMC-CEP-4017 does show evidence of orbital motion. In contrast, although SMC-CEP-0524 formally meets the $f_{\sigma, \text{cluster}}$ threshold, its RV measurements seems to follow a smooth and plausible RV curve at that pulsational period that the model does not accurately reproduce. Its SB1 nature hinges on the first temporal cluster, whose RV measurements sample phases not covered by the other clusters, preventing a direct comparison between epochs. After careful evaluation, we concluded that the star is probably not a binary but further observations would nevertheless be required to fully rule out binarity. In summary, we identified five binary Cepheids within the sample, including one new detection (SMC-CEP-4017), consistent with the expected number $E[N_{\text{SB1}}]$ (4 ± 2; Poisson error), previously determined.

The fit accuracy was found to be overall lower than for the LMC, with median and 90th percentiles *RMS E* values of 1.14 km s⁻¹ and 1.89 km s⁻¹, respectively. The increase in *RMS E* may be attributed to a combination of factors, including unaccounted instrumental offsets and/or discrepancy, unidentified binaries, period changes, and the larger metallicity difference relative to the VELOCE RV curve from which the priors were derived.

4.5. LMC and SMC kinematics traced by Cepheids

Figure 10 displays the spatial distribution of the analyzed Cepheids, color-coded by their systemic velocities in both galaxies tabulated in Tab. C.1. While the samples are small compared to targeted studies of LMC and SMC dynamics, some interesting features are evident. In the LMC, we find an interesting line-of-sight pattern across the field that resembles the rotation pat-

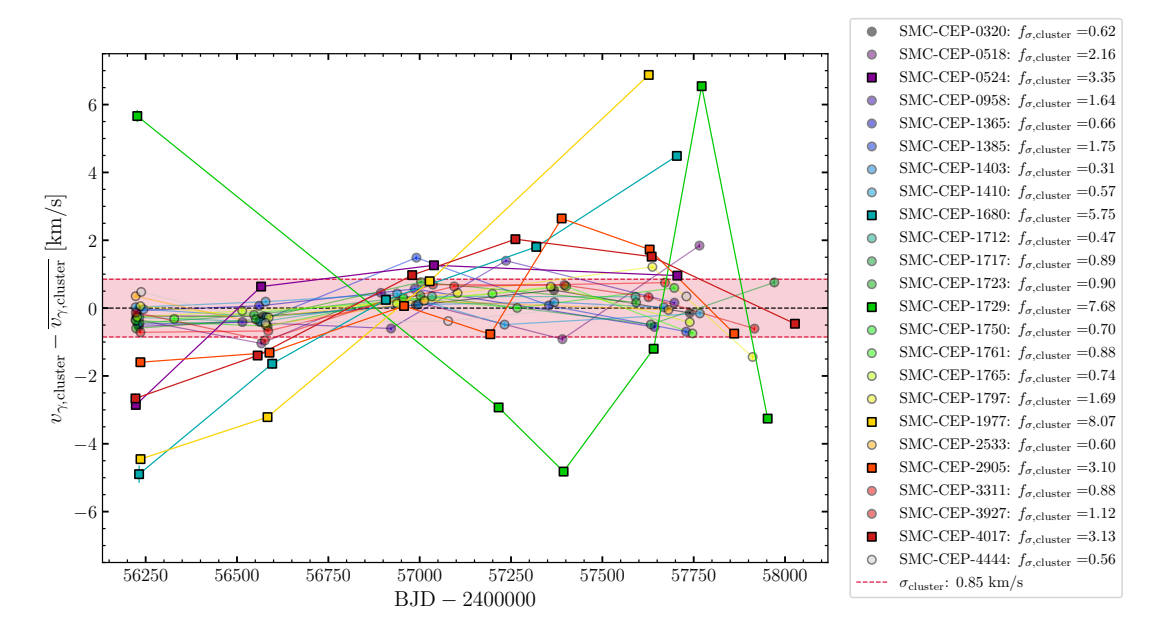


Fig. 9. Per target residuals of cluster-specific pulsation average velocities, $v_{\gamma,\text{cluster}} - \overline{v_{\gamma,\text{cluster}}}$, as a function of time for the SMC sample. The red shaded region indicate σ_{cluster} , while $f_{\sigma,\text{cluster}}$ values for each target are listed in the legend. Targets with $f_{\sigma,\text{cluster}} > 3$, the adopted threshold for identifying SB1 candidates, are marked with squares; all other targets are shown as circles.

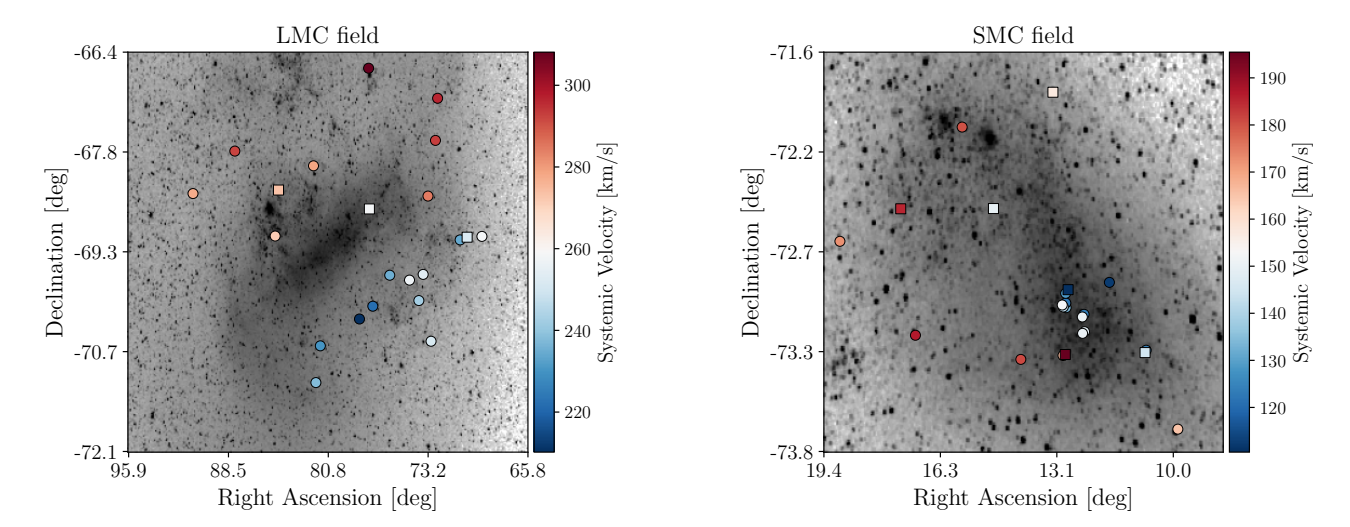


Fig. 10. Line of sight velocities of Cepheids across the LMC (left) and the SMC (right) as determined using observations from Storm et al. (2011) and Gieren et al. (2018). Spectroscopic binaries are shown using squares, other targets as circles. The line-of-sight systemic velocity is shown using a color scale. The background image was created using the *Melliger-Green* survey (Mellinger 2009) available from the astroquery.skyview python package (Ginsburg et al. 2019).

tern reported by detailed analyses from the literature (van der Marel & Kallivayalil 2014; Katz et al. 2022; Jiménez-Arranz et al. 2023). In the SMC, the spatial distribution of the Cepheids does not clearly indicate a large-scale rotation. However, we do note that several targets around $RA \sim 13.1 [\deg]$ may hint at a localized rotational pattern. The absence of a clear global rotation trend is consistent with the literature, which has established highly complex kinematics for the SMC, likely arising from tidal interactions with the LMC (e.g., De Leo et al. 2020). Further understanding the SMC's kinematics is thus of great interest for understanding the Magellanic system (cf. Zivick et al. 2021, and references therein). 4MOST will soon enable a detailed mapping of the line-of-sight velocity of many thousands of Cepheids that will be useful for understanding the dynamical

histories of both galaxies. The usefulness of Cepheids, specifically, in such endeavors derives from their relatively young ages (roughly 30 – 600 Myr), which can be determined precisely on a star-by-star basis using period-age relations (Anderson et al. 2016b), their high luminosity, which enables good RV precision, well-established LMC/SMC membership based on the Cepheid period-luminosity relation, and even the ability to constrain the position along the line of sight within each galaxy, especially within the elongated structure of the SMC (e.g., Scowcroft et al. 2016). Given the high accuracy achievable for individual Cepheids, we consider our methodology very promising to pursue highly detailed, population-specific kinematic studies of the Magellanic Clouds using 4MOST, which will begin survey operations in 2026.

5. Conclusions

We have developed a framework for accurately fitting Cepheid RV curves trained on PCA applied to the high-precision dataset from VELOCE-I. Our framework differs from a typical template fitting approach in that prior distributions of the RV curve coefficients are used to fit RV measurements instead of adopting fixed RV curve parameters for a given log *P*. Classical templates can be derived from our framework, e.g., by adopting the maximum of each prior distribution for a given log *P*, albeit at the cost of accuracy. The priors were derived by PCA and are published in electronic form alongside this article.

We extensively tested our methodology and found overall excellent performance, indicating that the PCs capture the Cepheid RV curves diversity in scale and morphology very well. Our method allows to determine v_{γ} (pulsation average velocities) to within a couple tens of m s⁻¹, slightly better than the per-epoch precision of the RV measurements used, and with no significant bias (mean offset of 5 m s⁻¹). Peak-to-peak amplitudes are usually recovered to within $\sim 2\%$. Limitations arising near the complex HP and in the case of peculiar Cepheids with unusually low amplitudes were discussed. The diversity of RV curve shapes in the interval $\log P \in [1, 1.3]$ prevents a unique mapping of RV curve shape based on period and results in larger differences of up to several % in P2P amplitudes, which tend to be biased low. Cepheids exhibiting unusually low P2P exhibit higher-thanusual RMSE.

By subsampling the VELOCE data set, we demonstrated that v_{γ} and P2P are typically recovered within 0.35 km s⁻¹ and 6-7%, respectively, from as few as 3 or 4 observations. This highlights the practical usefulness of our fitting framework in the context of large spectroscopic surveys, such as 4MOST.

Analyzing literature time-series RV measurements of Cepheids in the Magellanic Clouds, we obtained accurate RV curve fits with 90th-percentile RMS E values of $1.16 \,\mathrm{km}\,\mathrm{s}^{-1}$ for the LMC and $1.89 \, \mathrm{km} \, \mathrm{s}^{-1}$ for the SMC. We carefully determined the ability of our method and the available data to identify spectroscopic binaries. Using a hierarchical model, we identified several previously reported binary systems and three new detections (two in the LMC and one in the SMC). These detections lead to a lower limit of the SB1 fraction of Cepheids of $\sim 3/12 = 25\%$ in the LMC and $((5 + 2(\text{not analyzed})/24 \sim 29\%)$ for the SMC. However, we note that the Magellanic Clouds harbor a large population of double-lined spectroscopic binaries not seen in the Milky Way (Pilecki et al. 2021; Pilecki 2025). Detailed comparisons between the binary fractions of the Magellanic Clouds and the Milky Way, where 29% of Cepheids reside in SB1 systems (see VELOCE-II), will further benefit from our methodology and the upcoming 4MOST observations. Additionally, the spatial distribution of v_{ν} values determined for LMC Cepheids matches the expected line-of-sight component of its large-scale rotation. In the SMC, the situation appears to be more complex.

Our PCA-based framework provides a robust foundation for systematic investigations of Cepheid multiplicity and galaxy kinematics based on stellar sub-populations across the Milky Way and the Magellanic Clouds in the era of 4MOST and large ground-based spectroscopic survey. Future work will also consider extending this approach to RV time-series measurements from *Gaia*.

Acknowledgements. This work was supported by the European Research Council (ERC) under the European Union's Horizon 2020 research and innovation programme (Grant Agreement No. 947660). RIA is funded by the SNSF through an Eccellenza Professorial Fellowship, grant number PCEFP2_194638. This research has made use of the VizieR catalogue access tool, CDS, Strasbourg Astronomical Observatory, France (DOI: 10.26093/cds/vizier) (Ochsenbein et al.

2000). This research has made use of the SIMBAD database, CDS, Strasbourg Astronomical Observatory, France (Wenger et al. 2000). This research has made use of the Astrophysics Data System, funded by NASA under Cooperative Agreement 80NSSC21M0056. The analysis was conducted using the Python programming language and the related Jupyter Notebook application from the Project Jupyter². Our work mainly used the following opensource libraries: numpy (Harris et al. 2020), pandas (The pandas development team 2025), scikit-learn (Pedregosa et al. 2011b), statsmodels (Seabold & Perktold 2010), scipy (Virtanen et al. 2020), astropy (Astropy Collaboration et al. 2013, 2018, 2022), astroquery Ginsburg et al. (2019), emcee (Foreman-Mackey et al. 2013), matplotlib (Hunter 2007), and dill (McKerns et al. 2012; McKerns & Aivazis 2010-). We thank the developers for developing, maintaining and openly distribute these libraries. The authors thank the organizers of the RRLCEP-RR Lyrae & Cepheid Stars Conference 2024 (hosted by Cadi Ayyad University and Oukaimeden Observatory in Marrakesh, Morocco) for granting us the possibility to present this work's preliminary results.

References

Ablimit, I., Zhao, G., Flynn, C., & Bird, S. A. 2020, ApJ, 895, L12

Anderson, R. I. 2014, A&A, 566, L10

Anderson, R. I. 2016, Monthly Notices of the Royal Astronomical Society, 463, 1707

Anderson, R. I. 2019, A&A, 623, A146

Anderson, R. I., Casertano, S., Riess, A. G., et al. 2016a, ApJS, 226, 18

Anderson, R. I., Saio, H., Ekström, S., Georgy, C., & Meynet, G. 2016b, A&A, 591, A8

Anderson, R. I., Viviani, G., Shetye, S. S., et al. 2024, Astronomy & Astrophysics, 686, A177, publisher: EDP Sciences

Astropy Collaboration, Price-Whelan, A. M., Lim, P. L., et al. 2022, The Astrophysical Journal, 935, 167, publisher: IOP ADS Bibcode: 2022ApJ...935..167A

Astropy Collaboration, Price-Whelan, A. M., Sipőcz, B. M., et al. 2018, The Astronomical Journal, 156, 123, publisher: IOP ADS Bibcode: 2018AJ...156.123A

Astropy Collaboration, Robitaille, T. P., Tollerud, E. J., et al. 2013, Astronomy and Astrophysics, 558, A33, publisher: EDP ADS Bibcode: 2013A&A...558A..33A

Baranne, A., Queloz, D., Mayor, M., et al. 1996, A&AS, 119, 373

Barbey, K., Anderson, R. I., Viviani, G., et al. 2025, Astronomy & Astrophysics, 698, A287, publisher: EDP Sciences

Bassett, R. & Deride, J. 2019, Mathematical Programming, 174, 129

Bernstein, R., Shectman, S. A., Gunnels, S. M., Mochnacki, S., & Athey, A. E. 2003, in Society of Photo-Optical Instrumentation Engineers (SPIE) Conference Series, Vol. 4841, Instrument Design and Performance for Optical/Infrared Ground-based Telescopes, ed. M. Iye & A. F. M. Moorwood, 1694–1704

Bhardwaj, A., Kanbur, S. M., Marconi, M., et al. 2017, Monthly Notices of the Royal Astronomical Society, 466, 2805–2824, aDS Bibcode: 2017MN-RAS.466.2805B

Braga, V. F., Crestani, J., Fabrizio, M., et al. 2021, ApJ, 919, 85

Bras, G., Kervella, P., Mérand, A., et al. 2025, Astronomy and Astrophysics, 698, A97

Breuval, L., Riess, A. G., Casertano, S., et al. 2024, The Astrophysical Journal, 973, 30, publisher: IOP ADS Bibcode: 2024ApJ...973...30B

Cioni, M. . R. L., Storm, J., Bell, C. P. M., et al. 2019, The Messenger, 175, 54, aDS Bibcode: 2019Msngr.175...54C

Csörnyei, G., Szabados, L., Molnár, L., et al. 2022, MNRAS, 511, 2125

de Jong, R. S., Bellido-Tirado, O., Chiappini, C., et al. 2012, in Society of Photo-Optical Instrumentation Engineers (SPIE) Conference Series, Vol. 8446, Ground-based and Airborne Instrumentation for Astronomy IV, ed. I. S. McLean, S. K. Ramsay, & H. Takami, 84460T

De Leo, M., Carrera, R., Noël, N. E. D., et al. 2020, MNRAS, 495, 98

 Deb, S. & Singh, H. P. 2009, Astronomy & Astrophysics, 507, 1729–1737
 Dekker, H., D'Odorico, S., Kaufer, A., Delabre, B., & Kotzlowski, H. 2000, in Society of Photo-Optical Instrumentation Engineers (SPIE) Conference Series, Vol. 4008, Optical and IR Telescope Instrumentation and Detectors, ed.

M. Iye & A. F. Moorwood, 534–545 Dinnbier, F., Anderson, R. I., & Kroupa, P. 2024, A&A, 690, A385

Foreman-Mackey, D., Hogg, D. W., Lang, D., & Goodman, J. 2013, Publications of the Astronomical Society of the Pacific, 125, 306, publisher: IOP ADS Bibcode: 2013PASP.125..306F

Gaia Collaboration, Vallenari, A., Brown, A. G. A., et al. 2023, A&A, 674, A1 Gallenne, A., Kervella, P., Mérand, A., et al. 2017, A&A, 608, A18

¹ Python Software Foundation, https://www.python.org/

https://jupyter.org/

- Genovali, K., Lemasle, B., Bono, G., et al. 2014, Astronomy and Astrophysics, 566, A37, publisher: EDP ADS Bibcode: 2014A&A...566A..37G
- Gieren, W., Storm, J., Konorski, P., et al. 2018, Astronomy and Astrophysics, 620, A99, publisher: EDP ADS Bibcode: 2018A&A...620A..99G
- Ginsburg, A., Sipőcz, B. M., Brasseur, C. E., et al. 2019, The Astronomical Journal, 157, 98, publisher: IOP ADS Bibcode: 2019AJ....157...98G
- Hajdu, G., Dékány, I., Catelan, M., Grebel, E. K., & Jurcsik, J. 2018, The Astrophysical Journal, 857, 55
- Harris, C. R., Millman, K. J., van der Walt, S. J., et al. 2020, Nature, 585, 357, publisher: Nature Publishing Group
- Hocdé, V., Moskalik, P., Gorynya, N. A., et al. 2024, Astronomy and Astrophysics, 689, A224, publisher: EDP ADS Bibcode: 2024A&A...689A.224H
- Hocdé, V., Smolec, R., Moskalik, P., Ziółkowska, O., & Singh Rathour, R. 2023, Astronomy and Astrophysics, 671, A157, publisher: EDP ADS Bibcode: 2023A&A...671A.157H
- Hotelling, H. 1933, Journal of Educational Psychology, 24, 417
- Huang, Y., Fang, M., Liu, G., et al. 2024, Research in Astronomy and Astrophysics, 24, 075009
- Hunter, J. D. 2007, Computing in Science & Engineering, 9, 90
- Imbert, M., Andersen, J., Ardeberg, A., et al. 1989, Astronomy and Astrophysics Supplement Series, 81, 339, publisher: EDP ADS Bibcode: 1989A&AS...81..339I
- Jiménez-Arranz, Ó., Romero-Gómez, M., Luri, X., et al. 2023, A&A, 669, A91 Jin, S., Trager, S. C., Dalton, G. B., et al. 2024, MNRAS, 530, 2688
- Kanbur, S., Iono, D., Tanvir, N., & Hendry, M. 2002, Monthly Notices of the Royal Astronomical Society, 329, 126–134
- Kanbur, S. M. & Mariani, H. 2004, Monthly Notices of the Royal Astronomical Society, 355, 1361–1368, aDS Bibcode: 2004MNRAS.355.1361K
- Katz, D., Sartoretti, P., Guerrier, A., et al. 2022, arXiv e-prints, arXiv:2206.05902
- Kaufer, A., Stahl, O., Tubbesing, S., et al. 1999, The Messenger, 95, 8 Klagyivik, P. & Szabados, L. 2007, Astronomische Nachrichten, 328, 825,
- arXiv:0705.2138 [astro-ph]
 Klagyivik, P., Szabados, L., Szing, A., Leccia, S., & Mowlavi, N. 2013, Monthly
 Notices of the Royal Astronomical Society, 434, 2418, publisher: OUP ADS
- Bibcode: 2013MNRAS.434.2418K Kollmeier, J. A., Zasowski, G., Rix, H.-W., et al. 2017, SDSS-V: Pioneering
- Panoptic Spectroscopy, arXiv:1711.03234 [astro-ph]
- Liu, T. 1991, PASP, 103, 205
- Luck, R. E. & Lambert, D. L. 2011, The Astronomical Journal, 142, 136, publisher: The American Astronomical Society
- Mainieri, V., Anderson, R. I., Brinchmann, J., et al. 2024, The Wide-field Spectroscopic Telescope (WST) Science White Paper, arXiv:2403.05398 [astro-ph]
- Mayor, M., Pepe, F., Queloz, D., et al. 2003, The Messenger, 114, 20
- McKerns, M. M. & Aivazis, M. A. G. 2010-, pathos: a framework for heterogeneous computing
- McKerns, M. M., Strand, L., Sullivan, T., Fang, A., & Aivazis, M. A. G. 2012, Building a Framework for Predictive Science
- Mellinger, A. 2009, Publications of the Astronomical Society of the Pacific, 121, 1180, publisher: [The University of Chicago Press, Astronomical Society of the Pacific]
- Moe, M. & Di Stefano, R. 2017, ApJS, 230, 15
- Mróz, P., Udalski, A., Skowron, D. M., et al. 2019, ApJ, 870, L10
- Nardetto, N., Fokin, A., Fouqué, P., et al. 2011, Astronomy and Astrophysics, 534. L16
- Nardetto, N., Mourard, D., Kervella, P., et al. 2006, Astronomy & Astrophysics, 453, 309, publisher: EDP Sciences
- Nardetto, N., Stoekl, A., Bersier, D., & Barnes, T. G. 2008, Astronomy & Astrophysics, 489, 1255, publisher: EDP Sciences
- Netzel, H., Anderson, R. I., & Viviani, G. 2024, Astronomy & Astrophysics, 687, A118, publisher: EDP Sciences
- Netzel, H., Anderson, R. I., & Viviani, G. 2025, A&A, 694, A273
- Niederhofer, F., Cioni, M.-R. L., Schmidt, T., et al. 2022, MNRAS, 512, 5423 Ochsenbein, F., Bauer, P., & Marcout, J. 2000, Astronomy and Astrophysics Sup-
- plement Series, 143, 23
 Paul, S. & Chattopadhyay, T. 2022, arXiv e-prints, aDS Bibcode:
- 2022arXiv220108755P
 Pearson, K. 1901, The London, Edinburgh, and Dublin Philosophical Magazine and Journal of Science, 2, 559
- Pedregosa, F., Varoquaux, G., Gramfort, A., et al. 2011a, Journal of Machine Learning Research 12, 2875
- Learning Research, 12, 2825 Pedregosa, F., Varoquaux, G., Gramfort, A., et al. 2011b, Journal of Machine
- Learning Research, 12, 2825 Pilecki, B. 2025, Contributions of the Astronomical Observatory Skalnate Pleso, 55, 141
- Pilecki, B., Pietrzyński, G., Anderson, R. I., et al. 2021, ApJ, 910, 118
- Pont, F., Kienzle, F., Gieren, W., & Fouqué, P. 2001, Astronomy and Astrophysics, 376, 892, publisher: EDP ADS Bibcode: 2001A&A...376..892P
- Pont, F., Mayor, M., & Burki, G. 1994, A&A, 285, 415

- Prudil, Z., Smolec, R., Kunder, A., Koch-Hansen, A. J., & Dékány, I. 2024, A&A, 685, A153
- Prusti, T., Bruijne, J. H. J. d., Brown, A. G. A., et al. 2016, Astronomy & Astrophysics, 595, A1, publisher: EDP Sciences
- Ripepi, V., Clementini, G., Molinaro, R., et al. 2023, A&A, 674, A17
- Romaniello, M., Riess, A., Mancino, S., et al. 2022, Astronomy and Astrophysics, 658, A29, publisher: EDP ADS Bibcode: 2022A&A...658A..29R
- Scowcroft, V., Freedman, W. L., Madore, B. F., et al. 2016, ApJ, 816, 49 Seabold, S. & Perktold, J. 2010, in 9th Python in Science Conference Sesar, B. 2012, AJ, 144, 114
- Shetye, S. S., Viviani, G., Anderson, R. I., et al. 2024, Astronomy & Astrophysics, 690, A284, publisher: EDP Sciences
- Shlens, J. 2014, CoRR, abs/1404.1100 [1404.1100]
- Storm, J., Carney, B. W., Gieren, W. P., et al. 2004, Astronomy and Astrophysics, 415, 521, publisher: EDP ADS Bibcode: 2004A&A...415..521S
- Storm, J., Gieren, W., Fouqué, P., et al. 2011, Astronomy and Astrophysics, 534, A95, publisher: EDP ADS Bibcode: 2011A&A...534A...95S
- Szabados, L. & Klagyivik, P. 2012, Astronomy & Astrophysics, 537, A81, publisher: EDP Sciences
- Tanvir, N. R., Hendry, M. A., Watkins, A., et al. 2005, Monthly Notices of the Royal Astronomical Society, 363, 749–762
- The pandas development team. 2025, pandas-dev/pandas: Pandas
- Trahin, B., Breuval, L., Kervella, P., et al. 2021, A&A, 656, A102
- van der Marel, R. P. & Kallivayalil, N. 2014, ApJ, 781, 121
- Virtanen, P., Gommers, R., Oliphant, T. E., et al. 2020, Nature Methods, 17, 261, publisher: Nature Publishing Group
- Wenger, M., Ochsenbein, F., Egret, D., et al. 2000, Astronomy and Astrophysics Supplement Series, 143, 9, publisher: EDP ADS Bibcode: 2000A&AS..143...9W
- Yoachim, P., McCommas, L. P., Dalcanton, J. J., & Williams, B. F. 2009, The Astronomical Journal, 137, 4697
- Zivick, P., Kallivayalil, N., & van der Marel, R. P. 2021, ApJ, 910, 36

Appendix A: Principal Components

The six PCs obtained after applying PCA to the sampled VELOCE-I FS models, V^{FS} , are illustrated in Fig. A.1, cf. Sect. 3.1.

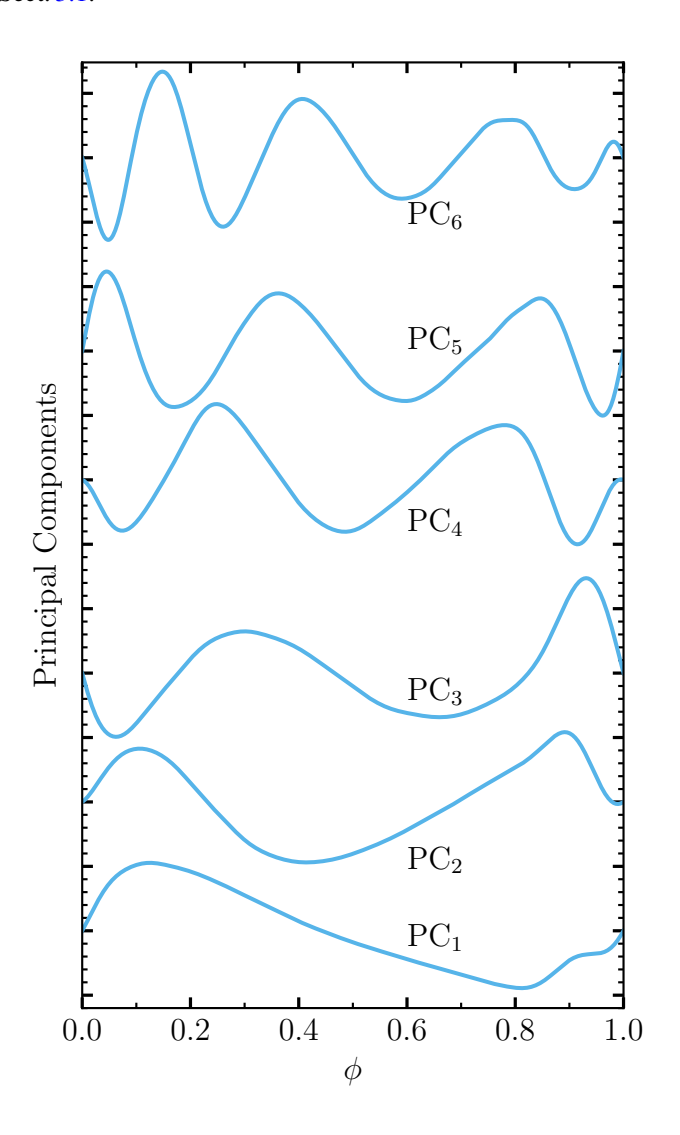


Fig. A.1. From bottom to top: the 6 PCs obtained by decomposing the VELOCE-I FS models, V^{FS} .

Appendix B: Results of fitting RV curves with varying number of RV measurements

In Sect. 3.3, we fitted the PCs (with the determined priors) to randomly selected $N_{\rm RV}$ measurements for each analyzed VELOCE-I Cepheid. The analysis was repeated for $N_{\rm RV}$ values ranging from 3 to 20, with results are reported in Tab. 1 and in Fig. 5 (for $N_{\rm RV}=3$). Here, we present the corresponding figures for $N_{\rm RV}=4$, 6, 10 and 20.

Appendix C: Results for the Magellanic Clouds

In Sect. 4, we applied our framework to RV measurements of Cepheids in the LMC and SMC, identifying SB1 candidates within the datasets. Here, we present the RV curve properties derived by fitting the $\mathcal{M}_{\text{RV}}^{\text{SOLO}}$ and $\mathcal{M}_{\text{RV}}^{\text{MULTI}}$ models.

Table C.1. Extragalactic Cepheids RV curve properties

	Storm et al. (20	011) LMC t	argets				
Target	$\overline{v_{\gamma, \mathrm{cluster}}}$	$P2P(v_{\gamma, \text{cluste}})$	er) P2P	RMS E			
	$[km s^{-1}]$	$[\mathrm{km}\mathrm{s}^{-1}]$	$[km s^{-1}]$	$[km s^{-1}]$			
HV873	251.21 ± 0.02	-	50.29	1.17 (2.3%)			
HV876	296.47 ± 0.02	-	62.31	0.82 (1.3%)			
HV877	292.86 ± 0.02	-	29.49	0.30 (1.0%)			
HV878	253.06 ± 0.02	-	59.78	0.68 (1.1%)			
HV881	242.36 ± 0.02	_	52.64	0.88 (1.7%)			
HV900	235.24 ± 0.02	_	47.19	0.56 (1.2%)			
HV914†	258.05 ± 0.77	3.91	40.33	1.06 (2.6%)			
HV1005†	273.67 ± 2.67		63.55	0.83 (1.3%)			
HV1006	271.75 ± 0.03		52.73	0.78 (1.5%)			
HV1023	291.64 ± 0.02		53.2	2.45 (4.6%)			
HV2282	256.79 ± 0.03		54.57	0.67 (1.2%)			
HV2369	308.11 ± 0.03		50.3	0.69 (1.4%)			
HV2405	210.19 ± 0.02		26.71	0.97 (3.6%)			
HV2527	230.44 ± 0.03		53.11	0.77 (3.6%)			
HV2538	278.29 ± 0.03		33.09				
HV2549				0.73 (2.2%)			
	237.91 ± 0.03		39.65	1.27 (3.2%)			
HV5655	222.00 ± 0.03		53.65	0.61 (1.1%)			
HV6093	277.20 ± 0.02		42.39	0.52 (1.2%)			
HV12452	234.23 ± 0.02		38.87	0.63 (1.6%)			
HV12505	284.73 ± 0.03		53.38	1.03 (1.9%)			
HV12717	258.23 ± 0.02		34.96	0.81 (2.3%)			
U1†	252.26 ± 1.69	6.29	61.44	0.59 (1.0%)			
Gieren et al. (2018) SMC targets							
SMC-CEP-0320	164.98 ± 0.01	-	13.43	0.33 (2.4%)			
SMC-CEP-0518	124.65 ± 0.02	-	52.73	1.40 (2.7%)			
SMC-CEP-0524	145.25 ± 0.03	-	32.27	1.19 (3.7%)			
SMC-CEP-0958	112.32 ± 0.01	-	55.66	2.13 (3.8%)			
SMC-CEP-1365	148.14 ± 0.01	-	22.39	0.65 (2.9%)			
SMC-CEP-1385	123.70 ± 0.02	-	36.03	1.09 (3.0%)			
SMC-CEP-1403	149.95 ± 0.01	_	32.27	0.68 (2.1%)			
SMC-CEP-1410	150.14 ± 0.03	_	47.43	1.83 (3.9%)			
SMC-CEP-1680†	110.51 ± 1.42		42.66	1.44 (3.4%)			
SMC-CEP-1712	133.32 ± 0.01	-	27.97	0.75 (2.7%)			
SMC-CEP-1717	122.40 ± 0.02	_	38.06	1.16 (3.0%)			
SMC-CEP-1723	128.74 ± 0.02		51.56	0.73 (1.4%)			
SMC-CEP-1729†	195.46 ± 1.82		51.17	2.17 (4.2%)			
SMC-CEP-1750	162.80 ± 0.01	-	57.29	0.87 (1.5%)			
SMC-CEP-1761	142.36 ± 0.01 142.36 ± 0.02		55.46				
	142.30 ± 0.02 166.73 ± 0.01	-		1.41 (2.5%)			
SMC-CEP-1765 SMC-CEP-1797		-	29.81	0.81 (2.7%)			
	152.36 ± 0.01	11.22	31.66	0.84 (2.7%)			
SMC-CEP-1977†	157.14 ± 2.21	11.33	19.19	1.32 (6.9%)			
SMC-CEP-2533	180.89 ± 0.02		34.06	1.66 (4.9%)			
SMC-CEP-2905†	149.50 ± 0.56		30.99	1.13 (3.6%)			
SMC-CEP-3311	180.12 ± 0.01		32.92	0.79 (2.4%)			
SMC-CEP-3927	186.67 ± 0.02		51.18	1.40 (2.7%)			
SMC-CEP-4017†	185.25 ± 0.68	4.69	45.01	1.91 (4.2%)			
SMC-CEP-4444	172.32 ± 0.01	-	56.82	1.04 (1.8%)			

Notes. Results of the application of the PC-based models to extragalactic Cepheids. The symbol \dagger highlights targets exhibiting evidence of orbital motion according to our analysis; for these stars, we report the results of the $\mathcal{M}_{\text{RV}}^{\text{MULTI}}$ fit and the P2P of the measured cluster-averaged velocities, $P2P(v_{y,\text{cluster}})$. For the rest of the targets, the results of the $\mathcal{M}_{\text{RV}}^{\text{MULTI}}$ fit are listed. The RMSE column gives, in parentheses, the RMSE-to-P2P ratio, indicating the relative strength of the residual scatter.

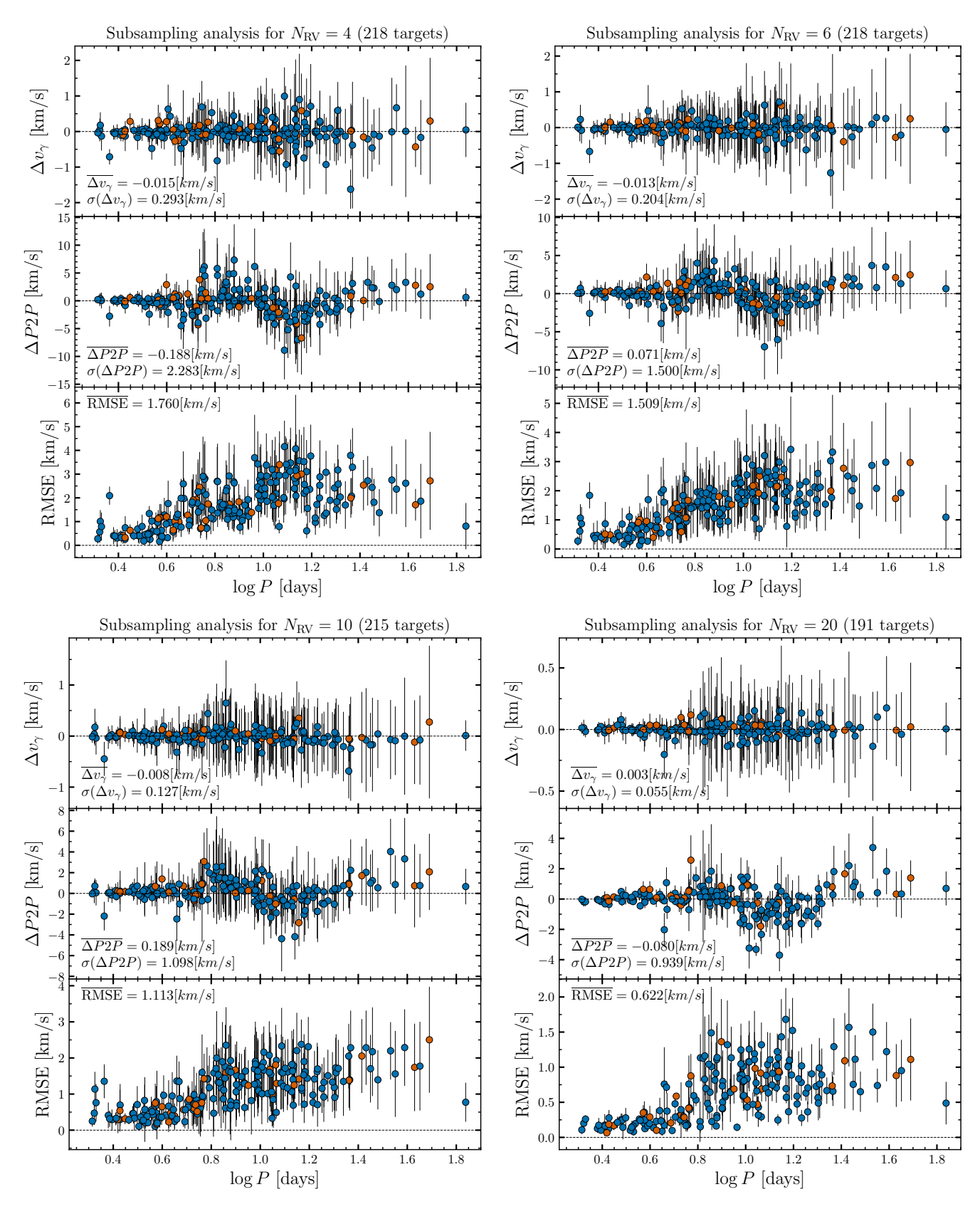


Fig. B.1. Performance of the PCs and priors applied to subsamples containing $N_{\text{RV}} = 4$, 6, 10 and 20 RV measurements. Each figure corresponds to one subsample size and displays, for each target, the mean and standard deviation of the results obtained for all combinations. From top to bottom, the statistics reported are: Δv_{γ} , $\Delta P2P$ and RMSE.